



Pre- and post-seismic deformation related to the 2015, M_w 7.8 Gorkha earthquake, Nepal



Adriano Gualandi ^{a,*}, Jean-Philippe Avouac ^{a,b}, John Galetzka ^c, Joachim F. Genrich ^a, Geoffrey Blewitt ^d, Lok Bijaya Adhikari ^e, Bharat Prasad Koirala ^e, Ratnamani Gupta ^e, Bishal Nath Upreti ^{f,g}, Beth Pratt-Sitaula ^h, Jing Liu-Zeng ⁱ

^a California Institute of Technology, Department of Geology and Planetary Sciences, Pasadena, CA, USA

^b University of Cambridge, Department of Earth Sciences, Cambridge, UK

^c UNAVCO Inc., Boulder, CO, USA

^d Nevada Bureau of Mines and Geology, University of Nevada, Reno, NV, USA

^e Department of Mines and Geology, Kathmandu, Nepal

^f Nepal Academy of Science and Technology (NAST), Khumaltar, Lalitpur, Nepal

^g Department of Geology, School of Mines, University of Zambia, Lusaka, Zambia

^h Geological Sciences Department, Central Washington University, USA

ⁱ State Key Laboratory of Earthquake Dynamics, Institute of Geology, China Earthquake Administration, Beijing 100029, PR China

ARTICLE INFO

Article history:

Received 13 February 2016

Received in revised form 7 June 2016

Accepted 9 June 2016

Available online 16 June 2016

Keywords:

Gorkha

Afterslip

ICA

Rate-strengthening

Pre-seismic

Post-seismic

GPS

ABSTRACT

We analyze time series from continuously recording GPS stations in Nepal spanning the pre- and post-seismic period associated to the M_w 7.8 Gorkha earthquake which ruptured the Main Himalayan Thrust (MHT) fault on April 25th, 2015. The records show strong seasonal variations due to surface hydrology. After corrections for these variations, the time series covering the pre- and post-seismic periods do not show any detectable transient pre-seismic displacement. By contrast, a transient post-seismic signal is clear. The observed signal shows southward displacements consistent with afterslip on the MHT. Using additional data from stations deployed after the mainshock, we invert the time series for the spatio-temporal evolution of slip on the MHT. This modeling indicates afterslip dominantly down-dip of the mainshock rupture. Two other regions show significant afterslip: a more minor zone up-dip of the rupture, and a region between the mainshock and the largest aftershock ruptures. Afterslip in the first ~7 months after the mainshock released a moment of $[12.8 \pm 0.5] \times 10^{19}$ Nm which represents $17.8 \pm 0.8\%$ of the co-seismic moment. The moment released by aftershocks over that period of time is estimated to 2.98×10^{19} Nm. Geodetically observed post-seismic deformation after co-seismic offset correction was thus $76.7 \pm 1.0\%$ aseismic. The logarithmic time evolution of afterslip is consistent with rate-strengthening frictional sliding. According to this theory, and assuming a long-term loading velocity modulated on the basis of the coupling map of the region and the long term slip rate of 20.2 ± 1.1 mm/yr, afterslip should release about $34.0 \pm 1.4\%$ of the co-seismic moment after full relaxation of post-seismic deformation. Afterslip contributed to loading the shallower portion of the MHT which did not rupture in 2015 and stayed locked afterwards. The risk for further large earthquakes in Nepal remains high both up-dip of the rupture area of the Gorkha earthquake and West of Kathmandu where the MHT has remained locked and where no earthquake larger than M_w 7.5 has occurred since 1505.

© 2016 Published by Elsevier B.V.

1. Introduction

The M_w 7.8 Gorkha earthquake of April 25, 2015 ruptured the Main Himalaya Thrust fault (MHT) near Kathmandu (Fig. 1). Details of the rupture kinematics have been very well constrained using near-field high-rate GPS measurements, SAR, and optical remote sensing as well

as seismological records (Avouac et al., 2015; Denolle et al., 2015; Elliott et al., 2016; Galetzka et al., 2015; Grandin et al., 2015; Kobayashi et al., 2015; Lindsey et al., 2015; Wang and Fialko, 2015). The earthquake initiated 75 km to the North-East of Kathmandu and propagated eastwards unzipping the lower edge of the locked portion of the MHT. It produced a rupture area about 150 km long along strike and 50 km wide located North of Kathmandu basin (Fig. 1). Pre- and post-seismic deformation was recorded at a number of permanent GPS stations which had been deployed before the mainshock. Some additional stations were deployed around the rupture area after the

* Corresponding author at: 1200 East California Boulevard, MC 100-23, Pasadena, CA 91125, USA.

E-mail address: gualandi@caltech.edu (A. Gualandi).

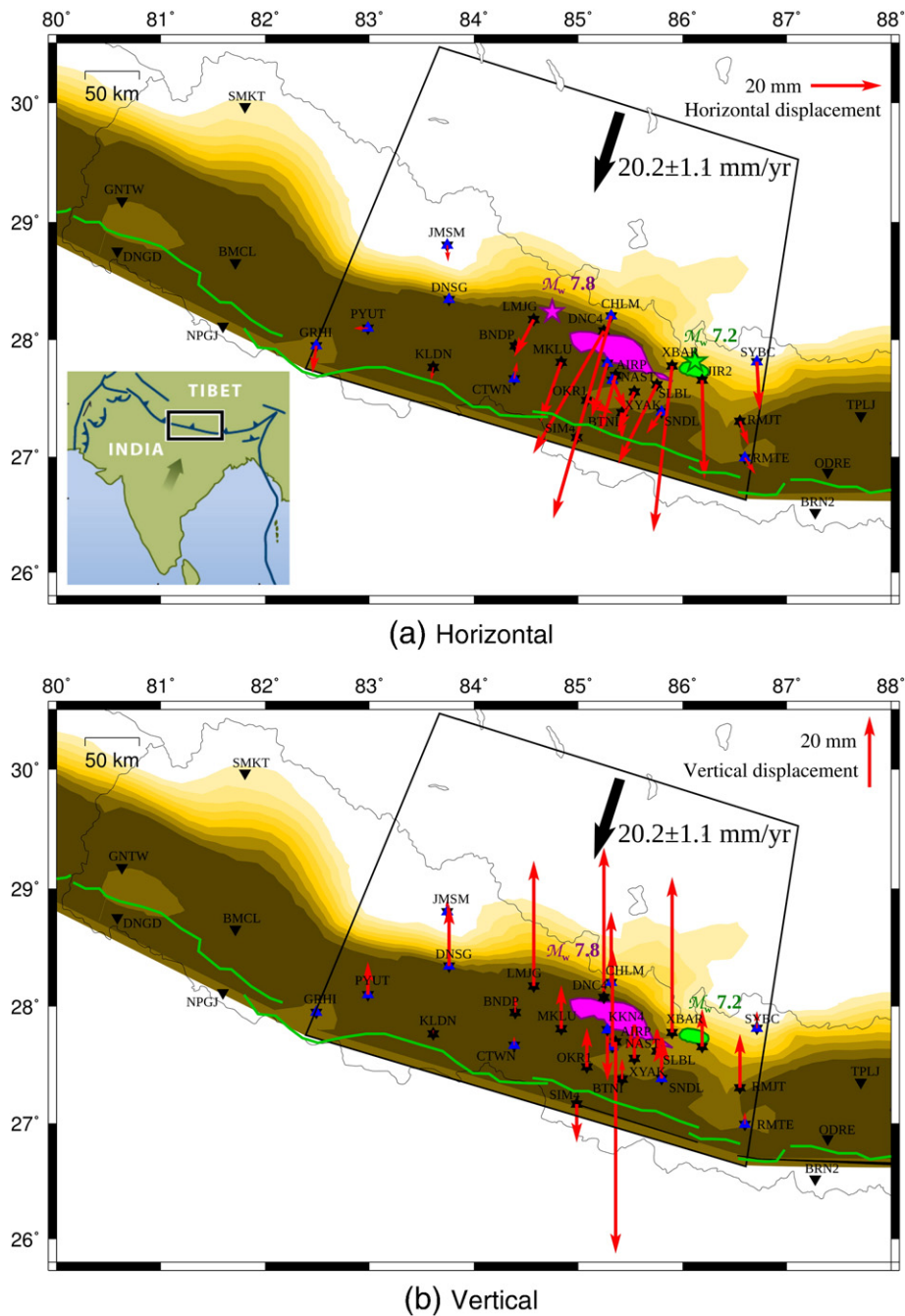


Fig. 1. (a) Post-seismic displacements and location of GPS stations used in this study relative to the rupture areas of the M_w 7.8 Gorkha earthquake of April 25th 2015 (magenta) and the M_w 7.2 aftershock of May 12th 2015 (green). Magenta and green stars: epicenters of mainshock and main aftershock, respectively. Magenta and green shadows: areas with more than 3 m of co-seismic slip during the mainshock and the May 12th aftershock, respectively (Galetzka et al., 2015). Black down-pointing triangles: stations used for the study of pre-seismic signal (column 4 Table 1). Blue up-pointing triangles: subset of stations used for the joint study of pre- and post-seismic signals (column 5 Table 1). Black up-pointing triangles: stations used for the study of only post-seismic signal (column 6 Table 1). Hexagons (up- and down-pointing triangles) show the stations in a radius of 300 km from the hypocenter. Black box: edges of MHT segment used for inversion of post-seismic signal. Yellow shadows: inter-seismic coupling map (Stevens and Avouac, 2015). Green line: fault trace at the surface (Styron et al., 2010). Red arrows: cumulative horizontal post-seismic deformation as retrieved by the first IC (see Section 2 for details), from day 2 to day 210 after the mainshock. Inset: map's footprint at regional scale. (b) as in (a), but for vertical displacement associated to first IC.

mainshock (Fig. 1). Hereafter we first describe this dataset and the techniques used to extract the transient pre- and post-seismic signals. Transient pre-seismic deformation, if present, is in the noise level. By contrast, post-seismic deformation is clear and reveals primarily afterslip. We next derive a model of the spatio-temporal evolution of afterslip. Finally, we compare this model with the pattern of inter-seismic locking of the MHT fault (Stevens and Avouac, 2015), co-seismic slip associated to the mainshock (Galetzka et al., 2015), the M_w

7.2 aftershock of May 12th 2015 and other aftershocks recorded by the local seismological monitoring (Adhikari et al., 2015), and discuss implications.

2. Data and signal extraction

Thirty-three permanent GPS stations had been deployed in Nepal before the mainshock by various institutions: the California Institute of

Technology (USA), the Department of Mines and Geology (Nepal), the Département Analyse et Surveillance de l'Environnement (CEA, France), the Nepal Academy of Science and Technology (Nepal), Central Washington University (USA), and Tribhuvan University (Nepal). Furthermore, some additional stations were deployed around the rupture area after the earthquake thanks to support from the National Aeronautics and Space Administration (NASA, USA), Department of Foreign International Development (UK), and Trimble Navigation Ltd. In addition, the data from three additional stations (AIRP, XBAR, and XYAK) deployed after the mainshock by Roger Bilham, Rebecca Bendick, and Ellen Knappe with funding from the National Science Foundation were also graciously made available to us. All these data can be downloaded from the UNAVCO website. The locations of all the stations used in this study are reported in Fig. 1 and Table 1.

We use the 24 h final solution daily GPS time series processed by the Nevada Geodetic Laboratory, University of Reno, Nevada. The time series are available at <http://geodesy.unr.edu/> (last accessed on January 27, 2016). The software used to process the GPS data is GIPSY/OASIS-II Version 6.1.1, developed at the Jet Propulsion Laboratory (JPL). The solution is obtained analyzing a worldwide network that includes RINEX data from several archives. The time series are in the IGS08 reference frame, and have been corrected for diurnal, semidiurnal, Mf, and Mm ocean tide loading using the tidal model FES04, while the semi-annual tidal

Table 1
Stations name and position. The symbols ✓ and ✗ indicate if a given station has been used for the corresponding analysis or not, respectively.

Station name	Longitude (°)	Latitude (°)	Pre-seismic study	Joint pre- and post-seismic	Post-seismic study
AIRP	85.3579	27.6972	✗	✗	✓
BMCL	81.7144	28.6558	✓	✗	✗
BNDP	84.3951	27.9495	✗	✗	✓
BRN2	87.2721	26.5196	✓	✗	✗
BTNI	85.4194	27.3797	✗	✗	✓
CHLM	85.3154	28.2054	✓	✓	✓
CTWN	84.3854	27.6683	✓	✓	✓
DNC4	85.2458	28.0770	✗	✗	✓
DNGD	80.5818	28.7545	✓	✗	✗
DNSG	83.7635	28.3451	✓	✓	✓
GNTW	80.6262	29.1765	✓	✗	✗
GRHI	82.4913	27.9509	✓	✓	✓
JIR2	86.1871	27.6570	✗	✗	✓
JMSM	83.7467	28.8044	✓	✓	✓
KKN4	85.2788	27.8008	✓	✓	✓
KLDN	83.6119	27.7669	✓	✗	✓
LMJG	84.5731	28.1740	✗	✗	✓
MKLU	84.8369	27.8100	✗	✗	✓
NAST	85.3277	27.6567	✗	✓	✓
NPGJ	81.5953	28.1172	✓	✗	✗
ODRE	87.3921	26.8662	✓	✗	✗
OKR1	85.0819	27.4844	✗	✗	✓
PYUT	82.9867	28.1014	✓	✓	✓
RMJT	86.5500	27.3051	✓	✗	✓
RMTE	86.5971	26.9910	✓	✓	✓
SIM4	84.9852	27.1657	✗	✗	✓
SLBL	85.7545	27.6190	✗	✗	✓
SMKT	81.8065	29.9694	✓	✗	✗
SNDL	85.7988	27.3849	✓	✓	✓
SYBC	86.7125	27.8142	✓	✓	✓
TPLJ	87.7098	27.3523	✓	✗	✗
XBAR	85.8998	27.7782	✗	✗	✓
XYAK	85.5384	27.5573	✗	✗	✓

loading as well as the solid Earth tide and pole tide have been corrected following the IERS (International Earth Rotation and Reference Systems Service) 2010 conventions. The Earth Orientation Parameters of the model have been calculated using the IERS 2010 conventions for diurnal, semi-diurnal, and long period tidal effects. We refer below to the downloaded time series as the 'raw' time series. We selected all the stations available in a radius of 1000km from the mainshock hypocenter, and we considered all the data in the time range [2010.0, 2015.8877], with the last epoch being the last available when we downloaded the data, and corresponding to the November 21, 2015.

Several processes are contributing to generate the displacements observed in the raw time series. Some are of tectonic origin, such as pre-, co-, post-seismic signals, the last being the one of interest in this study. There are other factors, including surface hydrology in particular. Previous studies have indeed shown that geodetic strain in the Himalaya shows significant seasonal oscillations induced by variations of continental water storage (Bettinelli et al., 2008; Fu and Freymueller, 2012; Chanard et al., 2014). In this study, we correct the raw time series for the offsets related to the mainshock (2015.3121) and the largest aftershock of May 12, 2015 (2015.3603) which reached M_w 7.2. The offsets related to the co-seismic displacements are estimated evaluating the average of the available positions 3 days after and before each offset, and removing the corresponding difference to all the data after the earthquake. We also correct the time series for a linear trend, representing secular inter-seismic deformation. The estimation of the linear trend is performed using the data from the pre-seismic stage from the beginning of 2010 to the mainshock [2010.0, 2015.3121].

The stations which recorded continuously before the mainshock are best suited for the analysis as the pre-seismic linear trend and seasonal variations can be estimated directly from the data and corrected for. Only 20 stations, out of 33, have more than 2 yr of data in the pre-seismic phase (column 4 Table 1), so that the amount of missing data for the whole network over the whole considered time span exceeds 50%. Among these 20 stations, 12 are located less than 300 km from the hypocenter (see hexagrams in Fig. 1). Two of them (KLDN and RMJT) did not record for months before the mainshock. Given that we cannot properly estimate the co-seismic offset at these stations, the number of continuous stations available for a joint study of pre- and post-seismic deformation is reduced to 10. We present the analysis restricted to this subset of stations in section S3 of the Supplementary Material, where we have also added NAST, even if it has only 1.23 yr of pre-seismic data, because of its strategic position (see column 5 Table 1 and blue triangles in Fig. 1). To carry out this study we used a modified version of the Principal Component Analysis-based Inversion Method (PCAIM) (Kositsky and Avouac, 2010), where we have introduced an Independent Component Analysis (ICA) decomposition (ICAIM). In particular, we adopt the variational Bayesian ICA approach (vbICA) of Choudrey (2002).

The vbICA algorithm assumes that i) a finite number of sources generates the observed data, ii) these sources are mixed linearly, and iii) the probability density function (pdf) related to the temporal evolution of a source is statistically independent from the pdfs of the other sources. The vbICA technique then allows us to determine the best reference frame onto which project the data in order to optimally separate the contribution of each singular source. We refer the interested reader to the Supplementary Material (Section S1) as well as to Choudrey (2002), Choudrey and Roberts (2003), and Gualandi et al. (2015) for more details. We preferred an ICA over a more standard PCA as a PCA does not do well at separating different sources of deformation (e.g. Kositsky and Avouac, 2010). In our case we tested the PCA approach and observed that most components were a mix of seasonal and post-seismic signals. By contrast, different sources of deformation, which tend to be statistically independent from one another, tend to be represented by different components in an ICA (Gualandi et al., 2015). This approach is thus particularly well suited to separate the contributions due to tectonics and surface hydrology. In the joint analysis of pre-

and post-seismic time series the seasonal strain due to surface hydrology and post-seismic relaxation are indeed clearly extracted and represented by different Independent Components (ICs), validating the idea that these two processes are independent (see Fig. S1 and Section S3 of the Supplementary Material). The results from the study of these continuous stations show that there is no detectable pre-seismic signal (see Sections 4 and S3). This analysis also serves as a sanity check of the post-seismic results presented in the main text which makes use of all the post-seismic data but could be biased due to the lack of constraints on the inter-seismic and seasonal components at a number of these stations. Figs. 2 and 3 show an example of detrended position time series used as input for the vbICA algorithm.

In order to extract the transient post-seismic signal and exploit all the data available during the post-seismic stage, including the stations deployed only after the mainshock, we have to correct the data for the linear and seasonal signals. A “trajectory model” (Bevis and Brown, 2014) would be a possible approach. For example, it is customary to model seasonal deformation as a combination of sinusoids, usually with imposed periods of 0.5 and 1 yr (e.g. Serpelloni et al., 2013). We did not adopt this approach because the seasonal contribution to the data might show interannual variations or might be not exactly annual and semi-annual. In addition, this approach cannot be applied to the

stations which were deployed after the mainshock, for which the “pre-seismic trajectory” cannot be constrained directly from the data. Another approach would be to predict the seasonal signal using measurements of surface load variations from the Gravity Recovery And Climate Experiment (GRACE) (Tapley et al., 2005). This approach has been proven successful (Bettinelli et al., 2008; Fu and Freymueller, 2012; Chanard et al., 2014) but it does not account well for spatial variability of the seasonal signal which can result from the limited (~400 km) spatial resolution of GRACE or local variations of the elastic response of the Earth due to sub-surface inhomogeneities or topographic effects. We therefore adopt another approach based directly on the ICA decomposition. The vbICA allows reducing the dataset to a linear composition of a limited number of sources each being associated to a spatial distribution and a temporal function. The technique is able to accommodate variations of the periodicity and amplitude of the seasonal signals as far as these signals are recorded by a sufficient number of stations. The trajectory model approach may be optimal in finding the best fit to any single time series considered in isolation, but with the vbICA approach we can estimate more consistently the regional response to a given source, and thus we think that we can interpolate the extracted signal with more confidence than if we were extrapolating a trajectory model at the stations deployed after the mainshock.

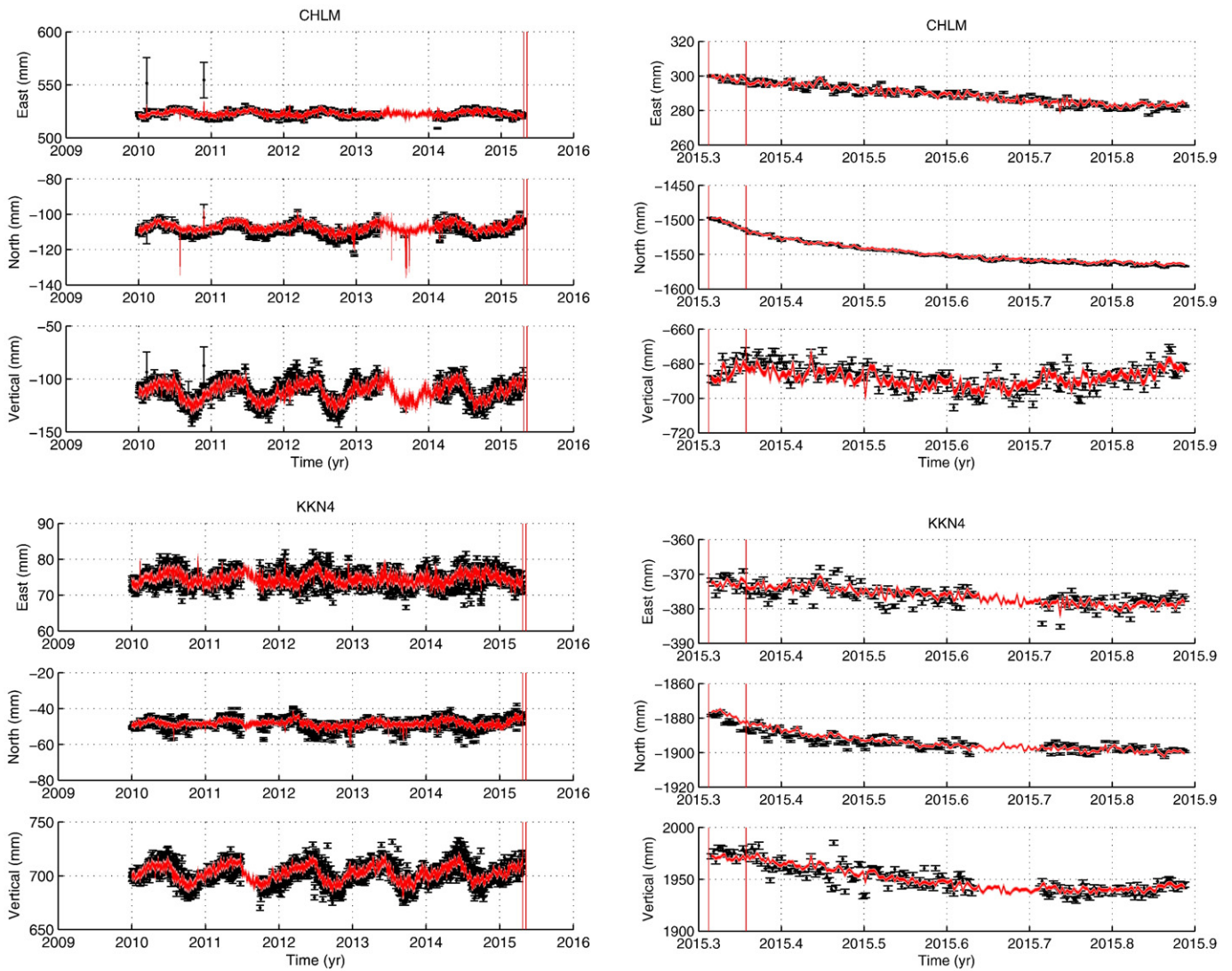


Fig. 2. Detrended position time series for stations CHLM and KKN4. We show the pre- and post-seismic stages separately (left and right panels) for the sake of clarity and better visualization of the post-seismic period. Red: ICA reconstruction for joint analysis of pre- and post-seismic deformation (Section 3 of Supplementary Material). The red vertical lines indicate the epochs of the mainshock and the largest aftershock.

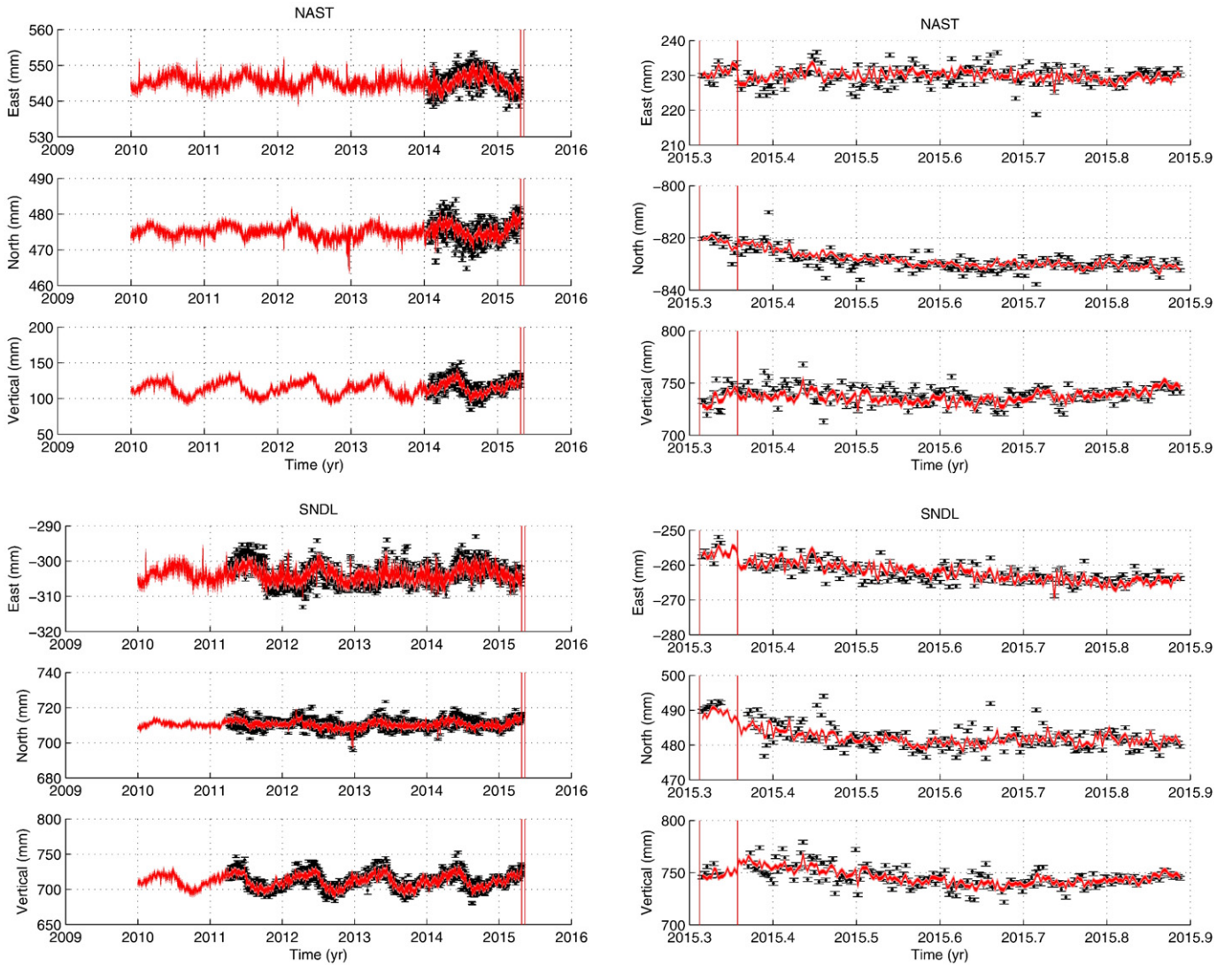


Fig. 3. As in Fig. 2, but for stations NAST and SNDL.

In practice we proceed as follows:

1. We apply the vbICA algorithm to the detrended pre-seismic time series at all the stations less than 1000 km from the hypocenter and having at least 2 yr of data in the time span from January 1st 2010 to April 25th 2015 [2010.0, 2015.3121] (see column 4 Table 1).
2. We extrapolate the pre-seismic ICs temporally in order to get the estimation at the post-seismic phase.
3. We interpolate the pre-seismic ICs spatial distribution at the stations that were deployed only after the mainshock.

Using a linear decomposition approach, like vbICA, we can thus perform just one spatial interpolation per component instead of one for every single epoch.

The vbICA analysis applied to the pre-seismic (detrended) time series yields that three ICs are optimal to reconstruct the time series, based on the Automatic Relevance Determination (ARD) criterion described in Gualandi et al. (2015) (point 1). The three ICs are shown in Fig. 4. The top of each panel shows the temporal evolution associated to each IC. The map views show the spatial distribution corresponding to each IC. Both the temporal and spatial values are non-dimensional. In the top-right corner of each map view we indicate the weight associated to each IC, in mm. To recompose the displacement time series $X_{M \times T}$, where M is the total number of time series (East, North, and Vertical for each station) and T is the total

number of epochs considered, it is necessary to multiply the spatial distribution u_i by the associated weight s_{ii} times the temporal evolution v_i^T , and then sum up the contributions from all the ICs. In matrix notation, we can thus write:

$$X_{M \times T} \approx X_{M \times T}^{ICA} = U_{M \times R} S_{R \times R} V_{R \times T}^T \quad (1)$$

where R is the number of ICs retained in the analysis.

The frequency analysis of the ICs shows that all of them have dominant frequencies at 1 and 2 yr^{-1} (see Fig. S9 of the Supplementary Material). To predict the temporal evolution of the ICs in the post-seismic phase (point 2), for every single IC we average the values separated by 365 days, and then we replicate the stacked value in the post-seismic stage. The choice of 365 days is dictated by the fact that the identified frequencies are multiples of 1 yr^{-1} . We are neglecting the effect of the shift in time due to the leap years since there is only one leap year in the considered time span (2012). The displacements observed at CTWN, GRHI, and NPGJ are not correctly represented by these three ICs though. The CTWN and NPGJ stations, which sit on alluvial sediments in the piedmont of the Himalaya, are clearly out-of-phase compared to all the other stations, probably due to poro-elastic deformation of the sediments. The GRHI station instead sits on a sandstone ridge in the piedmont, and is potentially affected by poro-elastic deformation as well.

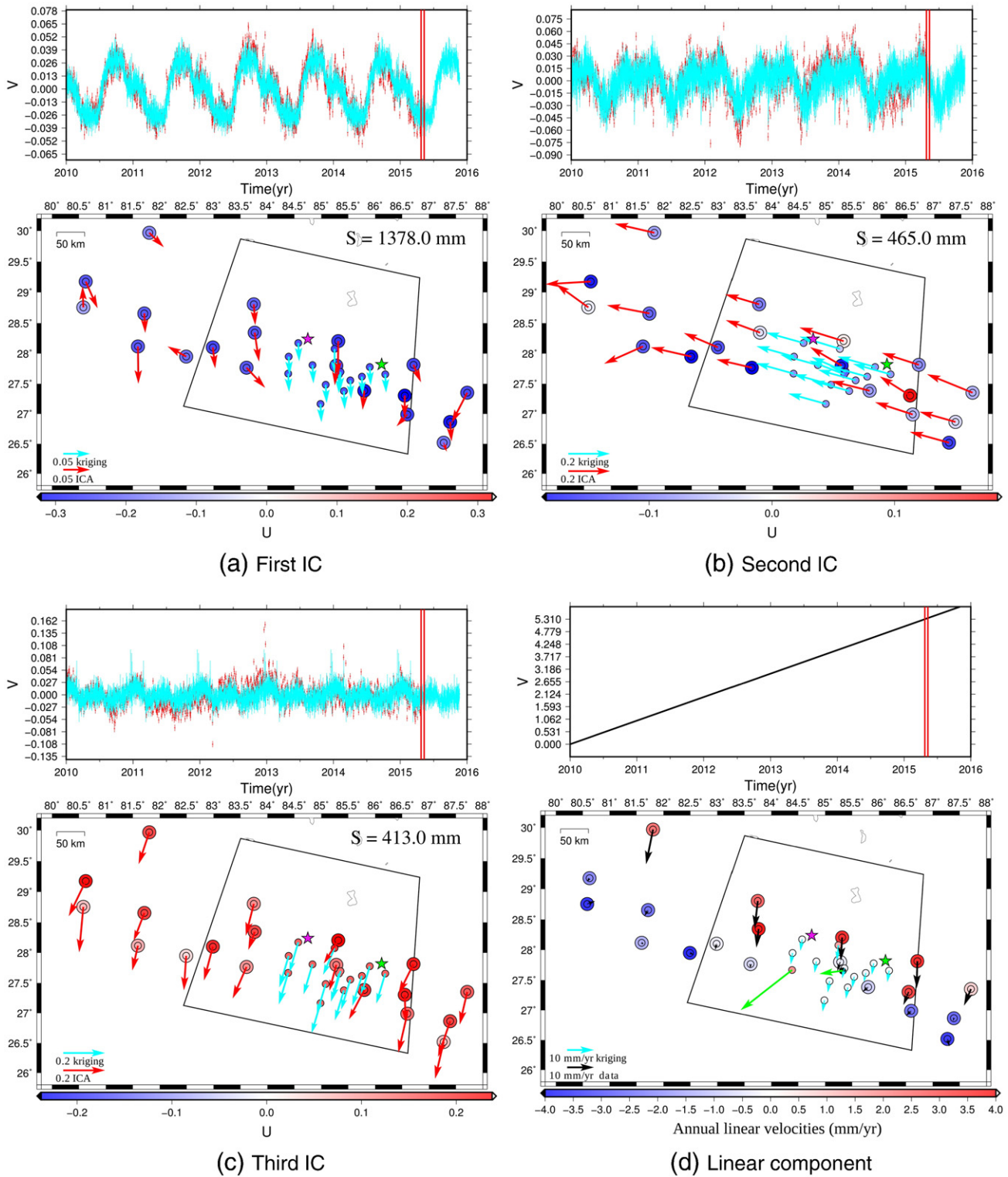


Fig. 4. Interpolated pre-seismic signal at stations deployed after the mainshock. Each panel shows the time function (top) and spatial distribution of surface displacements (bottom) associated to each of the ICs (a)–(c) and to the linear component (d). (a)–(c) The original time functions (red dots) are compared with yearly stacked time functions (cyan dots) associated to each IC. The two vertical red lines correspond to the times of the mainshock (M_w 7.8, April 25) and the largest aftershock (M_w 7.2, May 12). Stations represented by two circles are used for kriging. Colored circles show the vertical component of each distribution. Red arrows correspond to the horizontal spatial distribution of surface displacements deduced from the vblCA analysis. Cyan arrows correspond to the horizontal interpolated values. S value in the top-right corner: weight of the corresponding IC. (d) As in previous panels, but showing the velocity field. Black arrows: horizontal velocity field. Cyan arrows: horizontal interpolated field. Green arrows: horizontal velocity estimated at stations CTWN and NAST directly from the data and not used in the spatial interpolation of the linear trend. Black box and stars as in Fig. 1.

Therefore, we decided to treat these three stations independently modelling the seasonal signals by stacking the time series before the Gorkha earthquake.

To estimate the value of the ICs' field at the stations operating only during the post-seismic phase (point 3) we interpolate the spatial distributions represented by the U matrix of the ICA decomposition via a

kriging procedure. The weight S remaining the same, we reconstruct the predicted interpolated seasonal signal at all the stations as the linear combination of all the kriged spatial ICs and stacked temporal signals:

$$\chi^{est\ seasonal} = U^{krig} S V^{stack} \quad (2)$$

where $\chi^{est\ seasonal}$ is the estimated displacement, U^{krig} is the result of the kriging interpolation, S is the weight derived from the ICA decomposition, and V^{stack} contains the stacked temporal ICs. The estimated variance for U^{krig} is derived directly from the kriging analysis, while the variance for V^{stack} is calculated as the sample variance. The weights S are errorless scalars. The final uncertainties on the estimated values are calculated by propagating the uncertainties associated to U^{krig} and V^{stack} (see Section S2.1 of the Supplementary Material).

We proceed similarly for the estimation of the secular velocity field. For the 20 stations operating continuously in the pre-seismic stage we identify a long-term linear velocity. We notice that the station CTWN shows a long-term motion more than two times higher than the one of the stations around it for which we have data at our disposal. For this reason we prefer to exclude the velocity of CTWN from the velocity field adopted in the spatial interpolation procedure. We then kriged such velocity field on the location of the remaining stations, most of which were operating only in the post-seismic stage. The associated variance on the predicted position is estimated multiplying the squared expected value of the temporal signal times the variance of the velocity field. For the station NAST, used also in the joint analysis of the pre- and post-seismic signals, even if only 1.23 yr are available before the mainshock we prefer to use the velocity calculated from these pre-seismic data instead of the interpolated value.

We now have a predicted displacement for the seasonal and the linear signals at all the stations. We remove this predicted value, and we propagate the uncertainties onto the corrected time series considering the error sources independent from one another. Figs. S3–S8 of the Supplementary Material show the near field (less than 300 km from the hypocenter) continuous time series corrected for the long term linear trend calculated from the available pre-seismic data and for the co-seismic offsets (left panels) and corrected also for the seasonal components via the vICA decomposition (right panels). We limit the analysis to a subset of 25 out of 33 stations, corresponding to the near field stations (column 6 of Table 1). Considering only the post-seismic epochs reduces the percentage of missing data to ~21% for the subset of 25 stations. We can now consider these corrected time series to study the post-seismic deformation, whose temporal functions and spatial distributions are now better constrained thanks to the additional stations deployed after the mainshock.

We satisfactorily explain the data with three ICs (Fig. 5), where the first clearly represents post-seismic deformation. The second may contain some seasonal signal not properly corrected. Another possibility is that the first IC is capturing the afterslip related to the mainshock and the main aftershock, while the second IC would account for the difference between these two signals which cannot be properly separated. In order to clarify which interpretation is the correct one we need to study a longer time span, and we leave this analysis for the future, when more data will be available, including also stations from Tibet. The third IC is probably noise related to the network (including a Common Mode Error). Thus, for the moment we focus our attention on only the first component which unambiguously represents signal related to post-seismic deformation and which account for most of the measured post-seismic transient. In the next Section we show the results relative to the inversion of this component.

3. Inversion of the post-seismic deformation signal

The post-seismic displacements revealed by our analysis show clearly southward motion consistent with afterslip on the MHT. We therefore consider in our modelling that post-seismic deformation resulted

only from afterslip on the MHT. A joint inversion for afterslip and visco-elastic relaxation is left for future studies when longer time series and data from sites in southern Tibet will have become available. Having separated the post-seismic contribution of the deformation, we can perform a static inversion of the spatial distribution associated to it and combine the corresponding spatial distribution of the IC on the fault with the corresponding temporal function to retrieve the time evolution of slip on the fault. This procedure was first proposed and justified by Kositsky and Avouac (2010) using their PCA-based inversion method (PCA-IM). The approach is valid for any linear decomposition, and we can thus apply the same principle using an ICA decomposition. In order to perform the inversion we use a simple planar geometry. In particular, we use the central segment of the geometry defined by Stevens and Avouac (2015), and we extend the fault downdip (see black box in Fig. 1).

We slightly modified the inversion method of Radiguet et al. (2011) which follows the least squares formulation of Tarantola (2005) for linear problems. The a posteriori IC slip model m and the corresponding covariance matrix are given by:

$$\mathbf{m} = \mathbf{m}_0 + \mathbf{C}_{\mathbf{m}_0} \mathbf{G}^T (\mathbf{G} \mathbf{C}_{\mathbf{m}_0} \mathbf{G}^T + \mathbf{C}_{\mathbf{d}})^{-1} (\mathbf{d} - \mathbf{G} \mathbf{m}_0) \quad (3)$$

$$\mathbf{C}_{\mathbf{m}} = \mathbf{C}_{\mathbf{m}_0} - \mathbf{C}_{\mathbf{m}_0} \mathbf{G}^T (\mathbf{G} \mathbf{C}_{\mathbf{m}_0} \mathbf{G}^T + \mathbf{C}_{\mathbf{d}})^{-1} \mathbf{G} \mathbf{C}_{\mathbf{m}_0} \quad (4)$$

where \mathbf{m}_0 is the a priori model for the IC slip, $\mathbf{C}_{\mathbf{m}_0}$ is the a priori covariance matrix of the model parameters, \mathbf{G} is the matrix containing the Green's functions, \mathbf{d} is the data vector (i.e., the spatial distribution associated to the IC to be inverted), and $\mathbf{C}_{\mathbf{d}}$ is the covariance matrix of the data. As in Radiguet et al. (2011), we assume a null a priori model. If the data do not require slip at a certain location of the fault, then the a posteriori model will remain equal to the a priori model, i.e. equal to zero. We determine the least-squares solution given by Eq. (3) with an additional “positivity” constraint by imposing thrust motion, i.e. we solve for slip values having a rake in the range $[0^\circ, 180^\circ]$.

We use the formalism of Radiguet et al. (2011) for the a priori model covariance matrix, where an exponentially decaying spatial correlation is introduced. Given two patches **A** and **B** at a distance d_{AB} , the covariance element is given by:

$$C_{\mathbf{m}_0}^{AB} = \left(\sigma_{\mathbf{m}} \frac{\lambda_0}{\lambda} \right)^2 \exp\left(-\frac{d_{AB}}{\lambda} \right) \quad (5)$$

where λ controls the distance of the exponential decay, while $(\sigma_{\mathbf{m}} \frac{\lambda_0}{\lambda})^2$ is a weighting factor composed by a constant a priori standard deviation of the model parameters ($\sigma_{\mathbf{m}}$), and a scaling length factor fixed to the square root of the average subfault patches' area. We iteratively searched for the best value of the two parameters λ and $\sigma_{\mathbf{m}}$. We started with a constant $\sigma_{\mathbf{m}} = 0.5$ m, as in Radiguet et al. (2011), and tested several values for the parameter λ , ranging from 15 km ($\sim \lambda_0$, i.e. no correlation) to 200 km (high correlation). Because of the positivity constraint and the null a priori model, the inversion operates a compromise between the fit to the data, the smoothness of the slip distribution, and the sparsity of the slip distribution. As a result rougher models do not necessarily yield a better fit. We actually found an optimal λ value for which the misfit is minimum. We then fixed λ to this optimal value and searched for the best $\sigma_{\mathbf{m}}$ in the range 0.05 to 0.8 m (see values in Table 2). This iterative procedure converged to the final values of $\sigma_{\mathbf{m}} = 0.13$ m and $\lambda = 25$ km. Our best model, obtained using these two values, is referred to as Model 1 hereafter, and shown in Fig. 6. Figs. S10 and S11 of the Supplementary Material show the norm of the model vs the norm of the misfit for the different iterations. We also inverted the post-seismic IC obtained from the subset of stations indicated in column 5 of Table 1. We formally propagate the uncertainties on the spatial and temporal components of the ICs derived from the

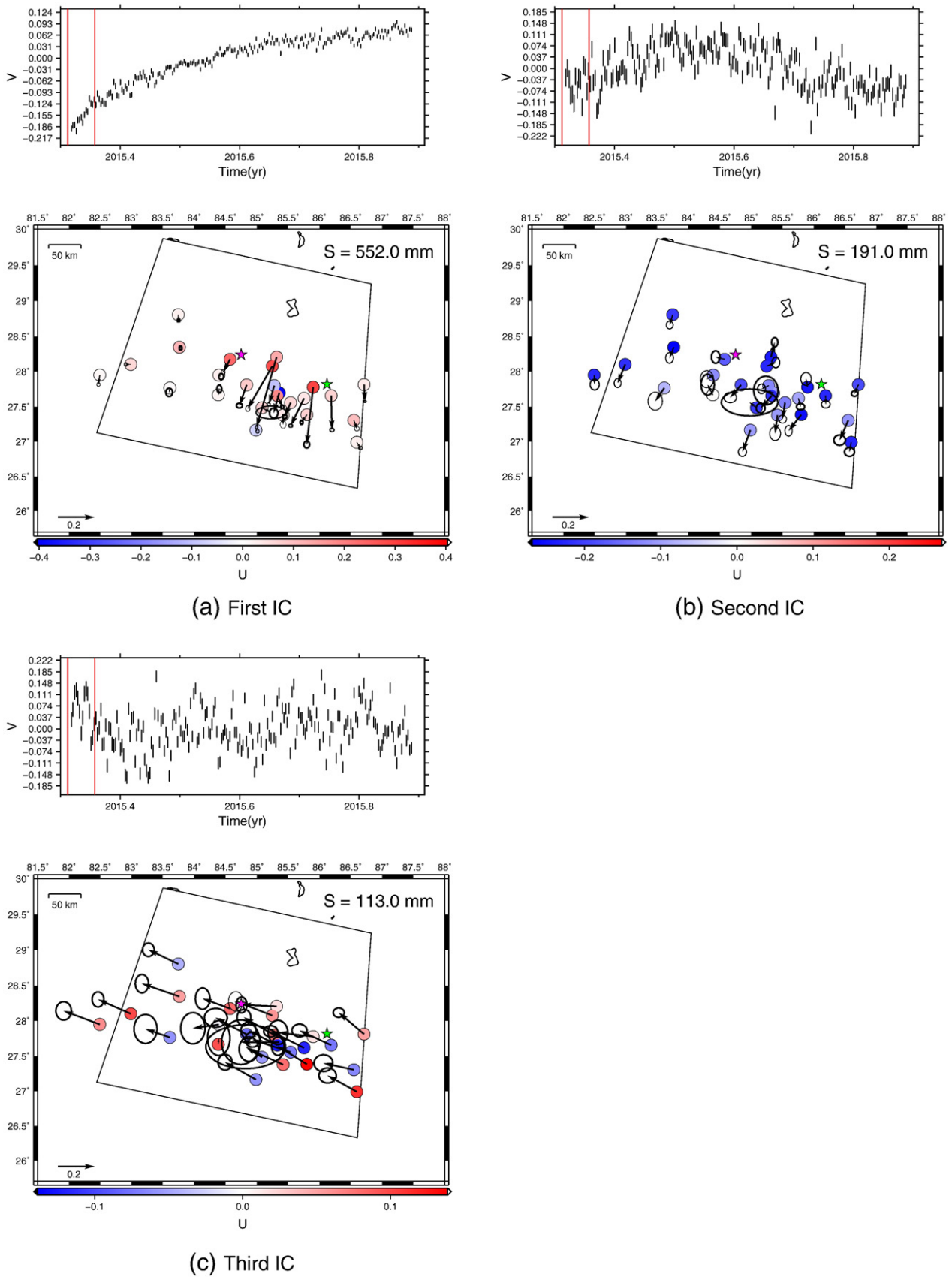


Fig. 5. Time function (top) and spatial distribution of surface displacements associated to each IC obtained from the vbICA decomposition of the post-seismic corrected time series (detrended, co-seismic offsets removed, and seasonal signals removed) at 25 continuous GPS stations (Model 1). The time span goes from April 27 to November 21, 2015 ([2015.3183, 2015.8877]). Colored circles show vertical component of each distribution. S : weight of each component. Stars as in Fig. 1.

Table 2
Tested values for the inversion parameters λ and σ_m . For the last two iterations searching for the best λ we have used the values of σ_m in the range 0.05–0.2 m with increasing steps of 0.01 m (see Figs. S10, S11, S19, and S20).

λ (km)	15	20	25	30	35	40	45	50	60	70	80	90	100	110	120	130	140	150	160	170	180	190	200	
σ_m (m)	0.05	0.1	0.15	0.2	0.25	0.3	0.35	0.4	0.45	0.5	0.55	0.6	0.65	0.7	0.75	0.8								

dispersion of the measurements to estimate the uncertainties on the time-dependent afterslip model (see Section S2 of the Supplementary Material). All the reported uncertainties correspond to the 1σ standard deviation estimation. The resulting model is presented in the Supplementary Material and referred to as Model 2 (see Section S3).

Model 1 shows a large afterslip patch down-dip of the co-seismic rupture (region A, Fig. 6). This large afterslip patch does not overlap with the co-seismic rupture areas of the mainshock and the May 12 aftershock. The afterslip distribution also shows a shallower slip patch (region B, Fig. 6) that seems to overlap with the western part of the co-seismic rupture. In Model 2 these two features are not distinguished, and form one single patch (see Fig. S17). A third patch undergoing afterslip is observed only in Model 1 (region C, Fig. 6). This is likely due to the lower number of GPS stations used to infer Model 2. Model 1 fits the horizontal displacements within 1σ uncertainties (see Fig. 7a and c). It does not fit the pattern of subsidence and uplift around the rupture area very accurately (see Fig. 7b and d, and Figs. S12a, S12f, and S13e of the Supplementary Material). It fails to match the subsidence at stations KKN4 and AIRP, above the rupture area, and the uplift at DCN4, North of the rupture, is underestimated. The station DNC4 was put in operation 56 days after the mainshock. It may be that the ICA reconstruction of the missing data is not accurate in these very first days, when most of the afterslip takes place. The stations AIRP and NAST lie on fluvio-lacustrine sediments and could be affected by seasonal poro-elastic effects. Our methodology to correct for seasonal variations would not be well suited in that case. For NAST we had data prior to the Gorkha earthquake to determine the long-term secular trend. AIRP was deployed after the mainshock and our interpolation of the linear trend may be inaccurate. Finally, the misfit at KKN4, which sits on bedrock, might be an indication that the assumed planar fault geometry is

not adequate to reconcile the vertical and horizontal displacements. A flat-and-ramp fault geometry has long been proposed for this area (e.g. Pandey et al., 1995) and argued for recently following observations related to the Gorkha earthquake (Elliott et al., 2016; Duputel et al., 2016). Alternatively, it might reflect anelastic deformation of the thrust sheet above the MHT. Whether due to aftershocks or aseismic processes, internal deformation could indeed explain some of the residuals that our best-fitting model fails to match. There is however no indication in the time series that this particular pattern of uplift and subsidence would be related to a specific aftershock. Fig. 8 shows the fit to 4 selected GPS stations. The remaining time series are shown in Fig. S12–S16 of the Supplementary Material.

From Model 1 we can calculate the moment released by afterslip in the time period that goes from the first to the last available data of the post-seismic phase $[t_1, t_{end}] = [2, 210]$ days, where we have excluded the first day after the mainshock because of possible artefacts due to an incomplete 24 h observation. The afterslip moment is calculated as:

$$M_{0[t_1, t_{end}]} = \sum_{p=1}^P \mu_p A_p (\tilde{\delta}_{as\ pt_{end}} - \tilde{\delta}_{as\ pt_1}) \quad (6)$$

where P is the total number of patches, μ_p is the rigidity modulus, and A_p is the area undergoing an afterslip $\tilde{\delta}_{aspt}$ at time t on the patch p as deduced from the data. According to regional seismological studies (e.g. Monsalve et al., 2008; Mahesh et al., 2013), the rigidity modulus may vary by up to 5 GPa in the depth range of our models. Assuming a uniform rigidity modulus $\mu = 30 \pm 5$ GPa, for Model 1 we find that afterslip released a moment of $M_{0[t_1, t_{end}]} = [9.2 \pm 1.1] \times 10^{19}$ Nm. The moment magnitude under the assumption of uniform rigidity modulus is

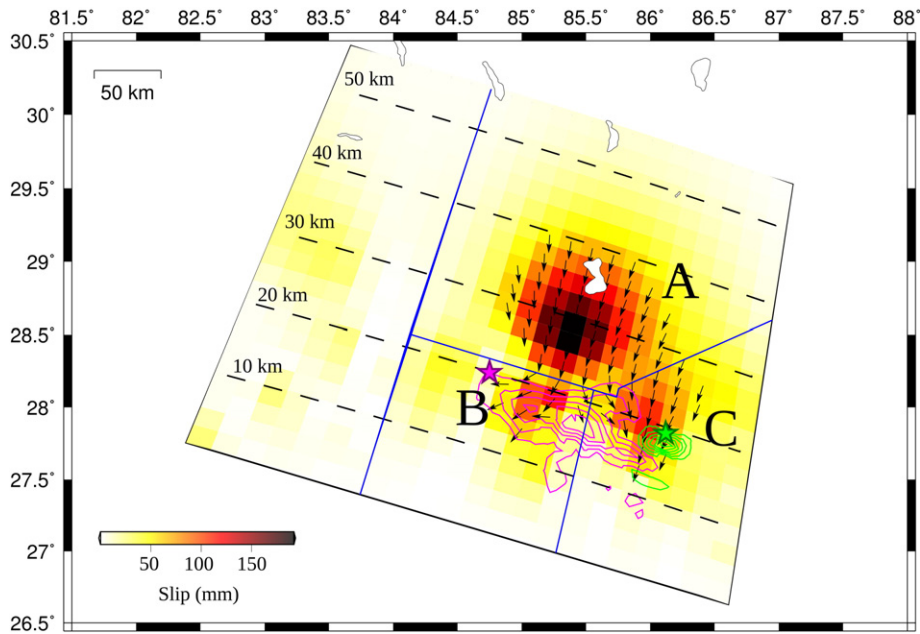


Fig. 6. Afterslip distribution (color palette) 210 days after the mainshock deduced from the inversion of first IC (see Fig. 5). Arrows: slip direction for patches with slip exceeding 25% of maximum slip. Magenta and green contour lines: mainshock and main aftershock co-seismic slip contours every 1 m from Galetzka et al. (2015). The three main regions of afterslip are delimited by blue polygons A, B, and C. Stars as in Fig. 1. The black dashed lines indicate the isodepth contours.

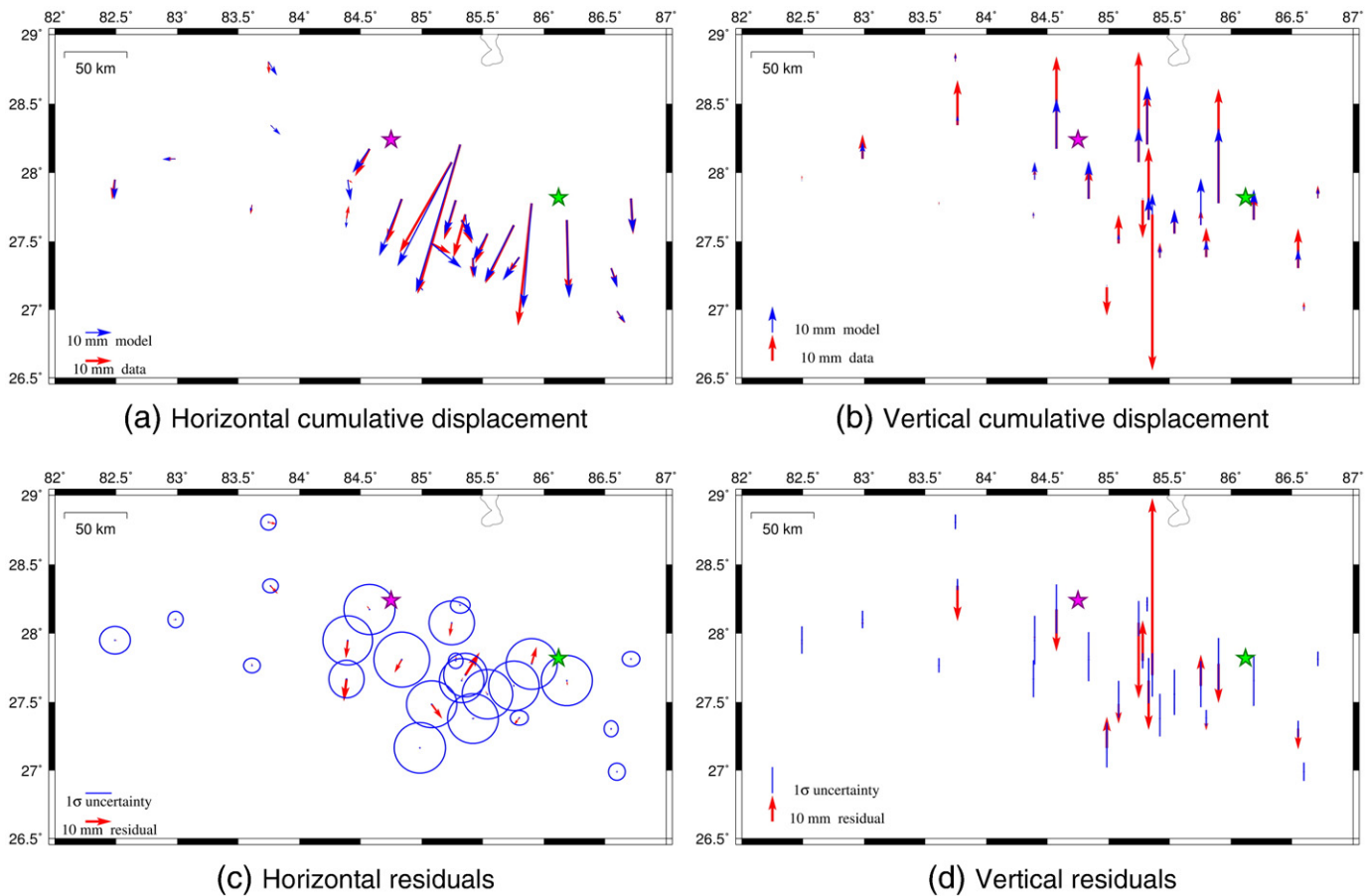


Fig. 7. Observed (red, as deduced from the first IC) and modelled (blue) horizontal (a) and vertical (b) cumulative displacements between April 27 and November 21, 2015. Horizontal (c) and vertical (d) residuals (red arrows) and 1σ uncertainties (blue ellipses and bars). Stars same as in Fig. 1.

estimated to be 7.24 ± 0.03 . Alternatively, we can introduce a dependency on depth of the rigidity modulus as in Galetzka et al. (2015). We make the hypothesis that the standard deviation on the determination of μ_p is increasing with the depth, so at every layer there is a different uncertainty associated. Moreover, we assume that the uncertainties at a given layer correlate between the patches belonging to the same layer. In other words, if the estimation of μ at a certain point is incorrect, then also the estimation at all the patches belonging to the same layer is incorrect by the same amount. Under this assumption, and using for the rigidity modulus the values in Table 3, we obtain that the measured moment released by afterslip is $M_{0[2,210]} = [12.0 \pm 0.9] \times 10^{19}$ Nm. The moment magnitude under the assumption of variable rigidity modulus is estimated to be 7.317 ± 0.020 . As we can notice, the assumption on μ_p distribution influences significantly the final estimation of the moment released. For the calculation in the following section we use the stratified model for the rigidity modulus.

4. Discussions

We used the data from the stations which were in operation before the Gorkha earthquake to search for an eventual pre-seismic signal. We considered either the 20 stations located at distances < 1000 km from the mainshock (pre-seismic analysis to correct stations with missing data), or focused on the 11 stations in the near field (< 300 km from the epicenter, see Section S3 of the Supplementary Material). We find that in both cases, the pre-seismic data are reconstructed within uncertainties (at the 1σ confidence level) from summing a linear inter-seismic component and a combination of seasonal components. The seasonal components could have absorbed a pre-seismic signal only if this had a spatial

distribution and time evolution similar to that of the regular seasonal variations which are known to be driven by surface hydrology. This seems improbable to us. Any pre-seismic signal should then show up in the residuals. The Root Mean Square of the residual of this analysis indicates that an upper bound for the eventual precursory signals is of 2 mm in the horizontal displacement component, and 7 mm in the vertical one. These values correspond to the typical noise level in daily GPS position time series used for tectonic geodesy. Visual inspection of the residuals at individual stations did not reveal any transient either (see Figs. S3–S8 in the Supplementary Material). Any transient would thus need to be in the noise level of the geodetic measurements.

We have shown that one IC dominantly represents post-seismic deformation (see Fig. 5). Since we have inverted only this component, the afterslip pattern is spatially stationary in our model. It is noteworthy that our model indicates relocking of the large slip (> 3 m) area of the Gorkha earthquake. Another robust feature of all the acceptable models obtained in this study is the deep patch of afterslip. In Model 1, which better constrains than Model 2 the post-seismic signal because of the higher number of active stations, the upper edge of the deep afterslip patch coincides approximately with the lower edge of the co-seismic rupture (Figs. 6 and 9). Most remarkably it also falls within the transition zone between the portion of the MHT that was fully locked prior to the mainshock and the creeping zone beneath the High Himalaya and southern Tibet (Figs. 6 and 9). The comparison of inter-seismic coupling with afterslip (Fig. 9) shows that afterslip compensates the gradient of inter-seismic creep at the lower edge of the locked zone. This observation is consistent with the inter-seismic partial locking of this zone being due to the stress shadow cast by the locked zone (e.g. Bürgmann et al., 2005; Hetland and Simons, 2010).

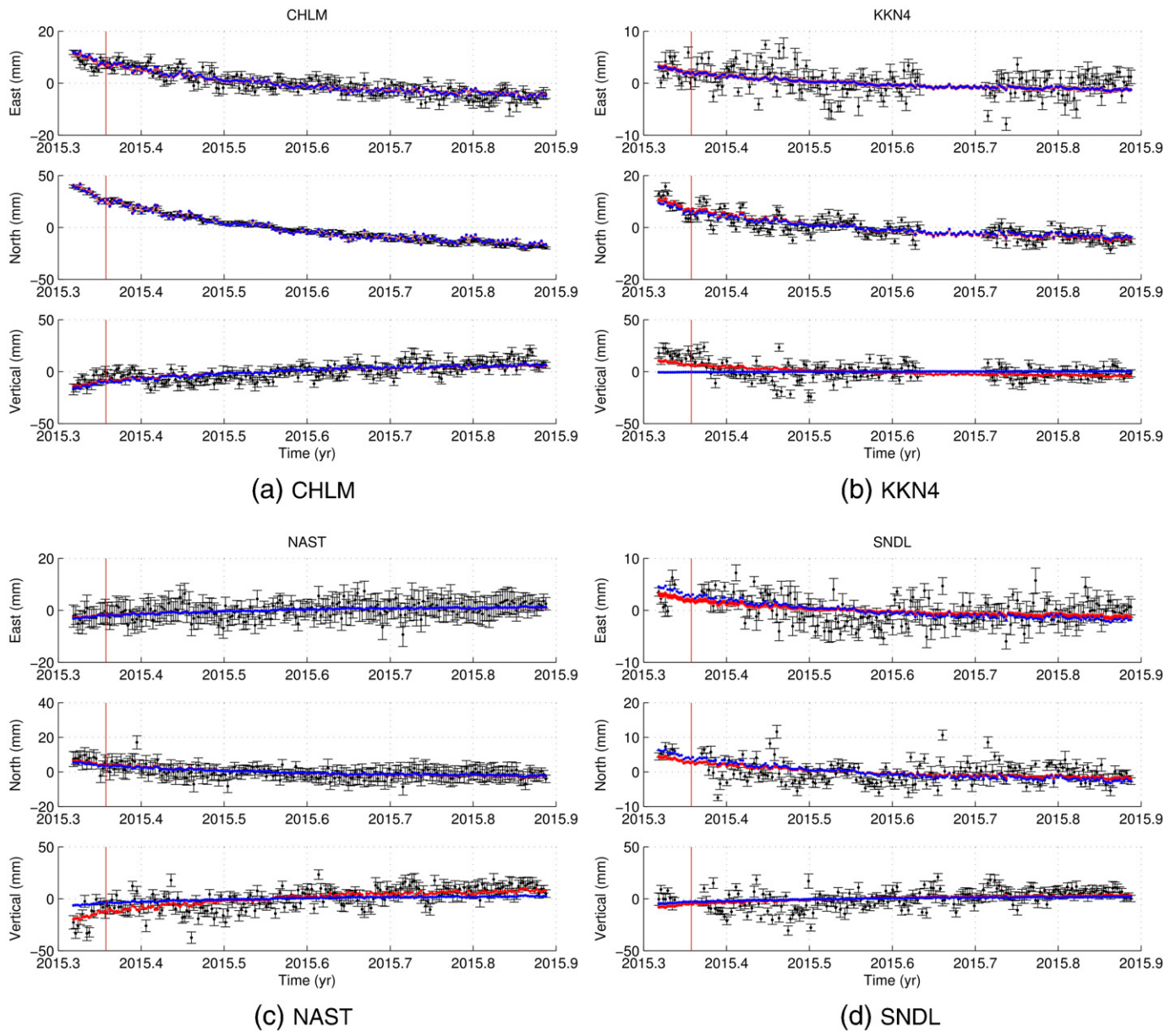


Fig. 8. Post-seismic position time series (black dots) at stations CHLM, KKN4, NAST, and SNDL after detrending and correction of co-seismic offset and seasonal variations. Red dots: contribution of the first IC (see Fig. 5). Blue dots: modelled displacements related to the first IC.

The recovered pattern of slip on the fault supports the conceptual model for which the creep gradient is compensated by afterslip in order to close the slip budget over the time of a seismic cycle. The northern extension of the deep patch of afterslip is not well constrained though due to absence of data from China. Similar deep afterslip has been observed following a number of large thrust events in subduction settings (e.g. Sun and Wang, 2015; Lin et al., 2013) and intracontinental settings (e.g. Hsu et al., 2002; Jouanne et al., 2011). The amount of deep afterslip in our models could be biased because our modelling ignores the potential contribution of viscoelastic relaxation. We have indeed assumed afterslip to be the dominant process in the near field of the

rupture for the early post-seismic. We show in the next paragraph that the temporal evolution of post-seismic deformation follows the highly non-linear relaxation pattern expected for afterslip governed by rate-strengthening frictional sliding. This observation adds further support to our claim that afterslip is the dominant post-seismic deformation mechanism.

To draw inference on the rheology governing deep afterslip we compare the time evolution of slip with prediction from frictional sliding. We resort to a simple 1-dimensional spring-slider system as has been used in a number of previous studies of afterslip (e.g. Marone et al., 1991; Perfettini and Avouac, 2004; Hsu et al., 2006; Perfettini et al., 2010). A more reliable estimate would require proper dynamic modelling of afterslip (e.g. Hearn et al., 2002; Perfettini and Avouac, 2007; Barbot et al., 2009), an approach left for future studies. We assume that friction varies only with the sliding rate, V_p , which is the expectation from rate-and-state friction models as the system evolves rapidly toward steady-state (Perfettini and Avouac, 2004; Perfettini and Ampuero, 2008) at a given patch p . The transient period over which

Table 3

Rigidity modulus (first line) and corresponding depths (second line) for the calculation of the moment released by the afterslip model.

μ (GPa)	25.9 ± 1.0	30.5 ± 1.5	33.0 ± 2.0	38.7 ± 2.5	43 ± 3
depth (km)	[0,4]	[4,15]	[15,20]	[20,27.5]	[27.5, ∞]

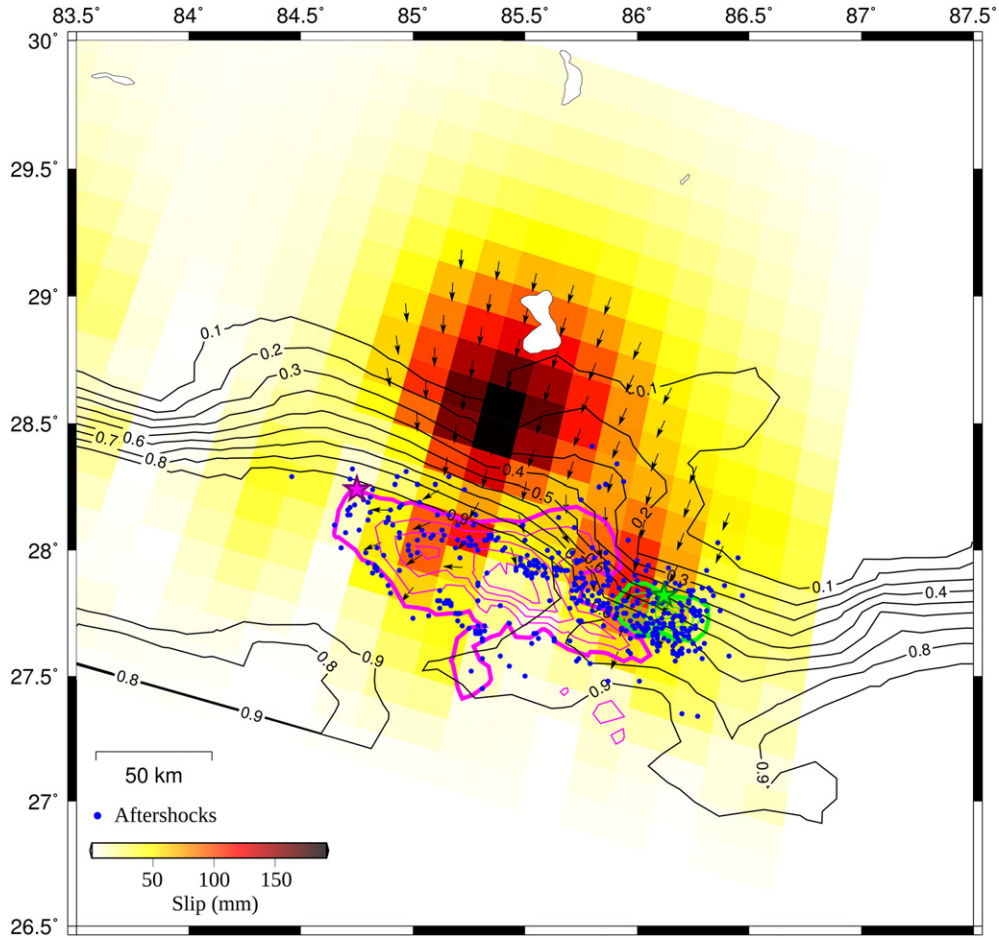


Fig. 9. Afterslip distribution (color palette and slip vectors as in Fig. 6), coupling contour lines (black) (Stevens and Avouac, 2015), mainshock and largest aftershock slip distribution contour lines every 1 m (magenta and green, respectively) (Galetzka et al., 2015). Blue dots: aftershocks from the NSC seismic catalogue. Stars same as in Fig. 1.

the state-variable might evolve is generally not observed in afterslip studies using daily time series, as we do here. The model predicts the time evolution of afterslip triggered by the co-seismic stress increase while submitted to stationary inter-seismic loading. The slip rate thus asymptotically decays to the long-term slip rate in that given patch (V_{0p}). Neglecting the interaction between patches, we can use the analytical solution of Perfettini and Avouac (2004) to predict the temporal evolution of afterslip. Given that afterslip is resolved starting only at time t_1 after the mainshock, the amount of slip until then is not known and is a parameter to be solved for. Following Gualandi et al. (2014), for the given patch p we use the equation (see Appendix A):

$$\frac{\tilde{\delta}_{as\ pt} - \tilde{\delta}_{as\ pt_1}}{V_{0p}} + (t - t_1) \approx \frac{\delta_{as\ pt} - \delta_{as\ pt_1}}{V_{0p}} + (t - t_1) = t_{rp} \ln \left[\frac{1 + q_p (\exp(t/t_{rp}) - 1)}{1 + q_p (\exp(t_1/t_{rp}) - 1)} \right] \quad (7)$$

where t is the time after the mainshock, $\tilde{\delta}_{aspt}$ is the transient afterslip as deduced from the data on patch p at time t , δ_{aspt} is the transient afterslip predicted by the model on patch p at time t . The total post-seismic deformation δ_{pt} will be given by the sum of the afterslip δ_{aspt} and the creep $V_{0p}t$. The left hand side of Eq. (7) is known, except for V_{0p} . The right hand side contains two parameters to be inverted for: the characteristic relaxation time t_{rp} and q_p , which relates the starting velocity of the slipping patch, the long-term velocity V_{0p} , and the stress variation due to the co-seismic slip distribution. These two parameters can be estimated once we choose V_{0p} , the asymptotic sliding rate after full relaxation. V_{0p} can be estimated based on the inter-seismic coupling model (Fig. 9) and the long term convergence rate V_0 which is estimated to be $20.2 \pm$

1.1 mm/yr in the study area (Stevens and Avouac, 2015). Given the uncertainty in the geometry of the dip-slip patch, V_{0p} is only approximatively estimated. For every given subpatch p we calculate the sliding rate as $V_{0p} = (1 - c_p)V_0$, where c_p indicates the coupling value at the desired location. We subsequently estimate the two parameters t_{rp} and q_p for every patch using a non linear least square fitting algorithm.

For the patch with maximum afterslip we find a relaxation time t_{rp} of 4.76 ± 0.05 yr (see Fig. 10a). The theoretical curve fits very well the estimated afterslip, suggesting that rate-strengthening friction, with a logarithmic dependence of friction on slip rate, is an appropriate rheology to account for our measurements of post-seismic deformation. We can next use the theoretical time-evolution of afterslip to calculate: 1) the amount of afterslip in the time between the mainshock and the first available data; and 2) the time evolution of the moment released by afterslip M_{0t} .

The afterslip produced by the model in the first two days after the mainshock released a moment of $[6.00 \pm 0.26] \times 10^{18}$ Nm. We can thus add this value to the estimated moment released over the interval [2,210] days to get the total M_0 released in the time span considered for the analysis. The added value represents $4.7 \pm 0.4\%$ of the total moment released by transient afterslip up to the last day of the analysis.

If we project the analysis over 100 yr after the mainshock, which is the order of magnitude of the return period of earthquakes similar to the 2015 event (Bollinger et al., 2014; Mugnier et al., 2013), we find that the maximum slip is 0.367 ± 0.025 m. We can also calculate the maximum asymptotic value of afterslip on each patch: $\delta_{aspt \rightarrow \infty} = \lim_{t \rightarrow \infty} \delta_{aspt} = V_{0p} t_{rp} \ln q_p$. In Fig. 10b the dashed green line corresponds

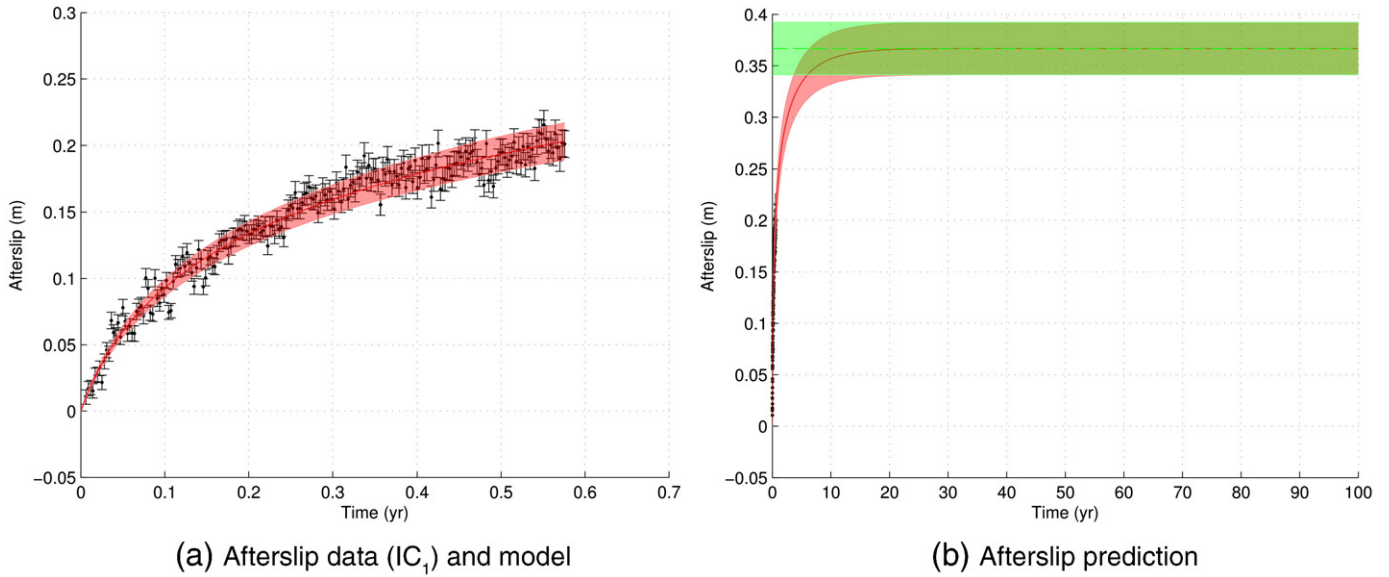


Fig. 10. (a) Afterslip, $\tilde{\delta}_{aspt} \pm \sigma_{\tilde{\delta}_{aspt}}$, on patch with maximum slip (black dots and errorbars) and model derived using Eq. (7), $\delta_{aspt} \pm \sigma_{\delta_{aspt}}$, to fit afterslip deduced from the first IC (red line and shadow). (b) Same as in panel (a), but with the afterslip projected over 100 yr after the mainshock. Green line and shadow: asymptotic afterslip value, $\delta_{aspt \rightarrow \infty} \pm \sigma_{\delta_{aspt \rightarrow \infty}}$.

to this value, while the red line is the model prediction based on the spring-slider analog model. We can now calculate the predicted moment released by afterslip. This quantity is shown in Fig. 11a. From the asymptotic afterslip on each patch we can reconstruct also the expected asymptotic maximum moment released by afterslip: $M_{0t \rightarrow \infty} = [24.5 \pm 1.0] \times 10^{19}$ Nm (green dashed line in Fig. 11), corresponding to a moment magnitude of $M_{wt \rightarrow \infty} = 7.523 \pm 0.012$. Our calculation indicates that after 100 yr afterslip will have released $95 \pm 5\%$ of the expected asymptotic value. The two major contributions to the uncertainty related to our estimate of the moment released by afterslip come from the uncertainty in the rigidity modulus and in the long-term creeping velocity (we neglect the uncertainties on the coupling map and of the area of each patch, as described in the Supplementary Material, Section S2). This prediction is based on the assumption that afterslip is the dominant deformation mechanism in the first 7 months after the mainshock. This is not a prediction of the total post-seismic deformation since other effects (e.g., viscoelastic relaxation) will likely play a more significant role over time.

The seismic moment released by the mainshock corresponds to $M_0^{\text{mainshock}} = 72 \times 10^{19}$ Nm (Avouac et al., 2015). This means that, after full relaxation, our afterslip model will have released $34.0 \pm 1.4\%$ of the moment released by the mainshock. According to our model, at the time of the last epoch available in the dataset (2015.8877), the afterslip released $[12.8 \pm 0.5] \times 10^{19}$ Nm, corresponding to $52 \pm 4\%$ of the asymptotic moment and to $17.8 \pm 0.8\%$ of $M_0^{\text{mainshock}}$. Based on the Global Centroid Moment Tensor (GCMT) catalogue (<http://www.globalcmt.org/>, Dziewonski et al., 1981; Ekstrom et al., 2012), the seismic moment released by aftershocks up to that same date (excluding the May 12 aftershock as the position time series were corrected for the corresponding offset) is 2.864×10^{19} Nm, and corresponds to only $22.4 \pm 1.0\%$ of the moment released by the afterslip model over the same time span. This is an underestimation of the seismic moment released by the entire aftershock sequence, since it has been calculated using only the large events for which a moment tensor could be calculated from modelling long period surface waves. Assuming the aftershocks to follow the Gutenberg–Richter distribution, it is possible to set an upper bound to the total seismic moment released by the seismic sequence.

Considering a local b -value of the Gutenberg–Richter law equal to 1.0 (Ader et al., 2012), and assuming that the GCMT catalogue is complete over magnitudes >5 , we find that an upper bound for the moment released by the aftershock sequence (excluding the May 12 aftershock) is 2.984×10^{19} Nm (see Appendix B), corresponding to $23.3 \pm 1.0\%$ of the moment released by the afterslip model over the same time span (where we are considering only the uncertainty on the moment released by afterslip to get the final uncertainty). Our afterslip model includes the effects of both seismic and aseismic contributions. We will still refer to our model as “afterslip model”, but it is important to keep in mind that the surface displacement used to deduce the model is potentially affected also by the aftershocks of minor intensity. Considering only aftershock and afterslip as post-seismic processes, we obtain that during the post-seismic phase at the very least $76.7 \pm 1.0\%$ of the moment released is aseismic, making afterslip the dominant mechanism of deformation. In Fig. 11c we compare the temporal evolution of the cumulative number of aftershocks corrected for the background rate estimated from the pre-seismic catalogue (completeness magnitude $M_L = 4.0$; National Seismological Center, NSC, seismic catalogue, <http://www.seismonepal.gov.np/>; see also Adhikari et al. (2015)) and the normalized curve of the evolution with time of the moment released by afterslip. We notice a slight discrepancy between the two curves that might be due to the fact that we have neglected the contribution of the second IC (see Fig. 11c) in the estimation of the afterslip model. It is possible that Model 1 is capturing the cumulative effects of both the afterslip related to the mainshock and the main aftershock. Only with longer time series we will be able to verify if the second IC is a tectonic signal or it is due to a miscorrection of the seasonal contribution. We leave for further studies the more in-depth investigation of the relationship between seismic and aseismic slip, as well as the study of the relation to fault friction properties.

A remarkable feature shows up when the afterslip pattern is compared with both the seismic ruptures and aftershocks. We see that the deep afterslip patch (region A, Fig. 6) reaches to shallower depth in the East, continuing in a patch that seems to extend in the narrow band between the eastern end of the mainshock rupture and the rupture of the May 12 aftershock (region C, Fig. 6). This area which was

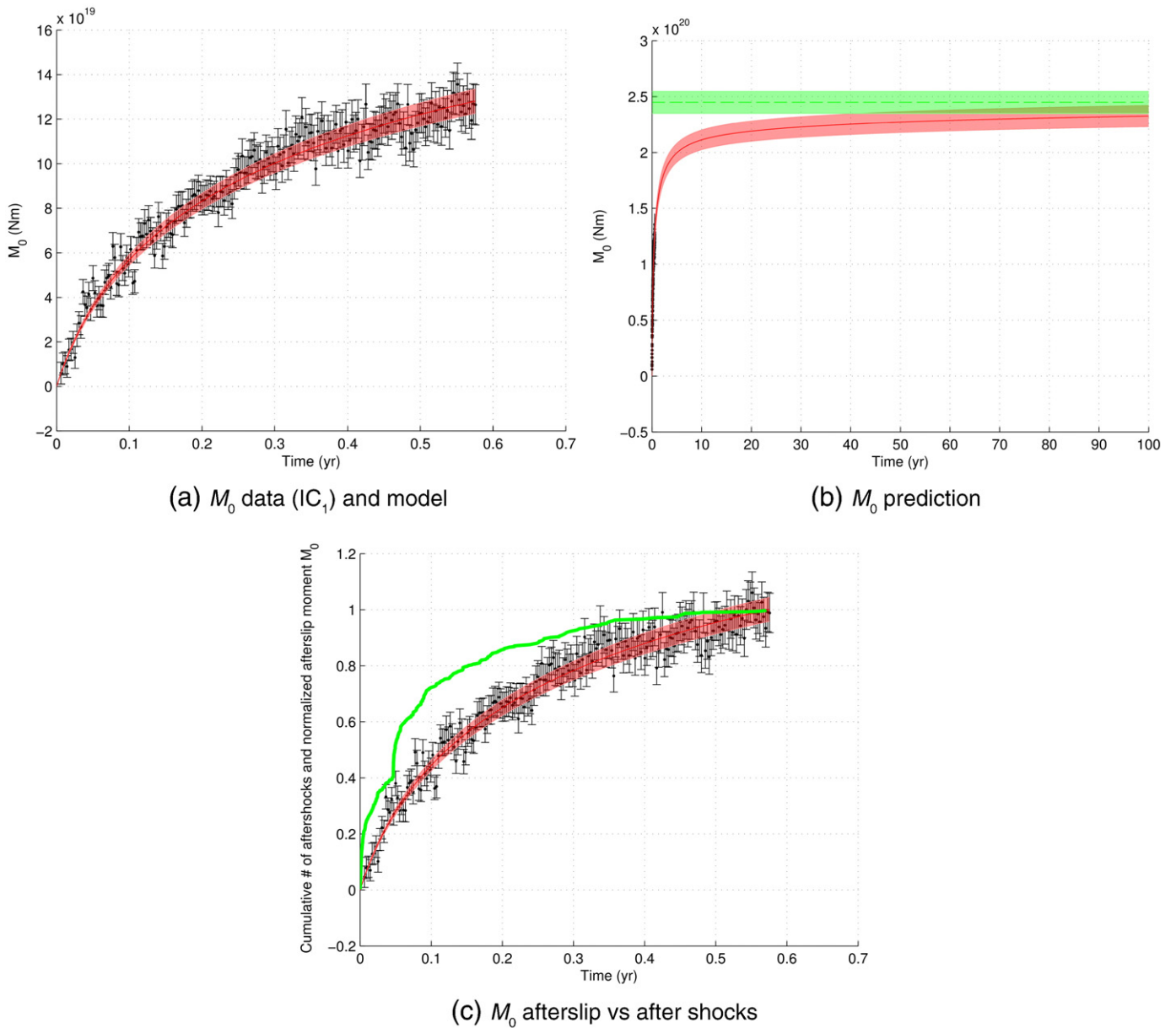


Fig. 11. (a) Moment, $\tilde{M}_{0t} \pm \sigma_{\tilde{M}_{0t}}$, released by afterslip (black dots and errorbars) compared with prediction, $M_{0t} \pm \sigma_{M_{0t}}$, from Eq. S21 of the Supplementary Material (red line and shadow). (b) Same as in panel (a), but projected over 100 yr after the mainshock. Green line and shadow: asymptotic moment value, $M_{0t \rightarrow \infty} \pm \sigma_{M_{0t \rightarrow \infty}}$. (c) Same as in panel (a), but normalized at the value of M_0 at the last epoch available (November 21, 2015). Green line: normalized cumulative number of aftershocks from the NSC seismic catalogue.

reloaded by afterslip also correlates with the zone of most intense aftershock activity (see Fig. 9). We thus propose that the mainshock eastward rupture arrested as it reached a rate-strengthening patch (such patches are known to act as barrier to seismic rupture propagation; Kaneko et al., 2010) and that afterslip in that zone and downdip of the rupture reloaded the shallower portion of the MHT triggering aftershocks, including the M_w 7.2 event of May 12, 2015.

Our study has also implications with regard to the seismic hazard potential of the MHT at the regional scale. We find that negligible aseismic slip occurred on the previously locked portions of the MHT. It follows that not much of the elastic strain available due to inter-seismic strain build up was released by post-seismic deformation. Actually the deep patch of afterslip must have contributed to rapid reloading of the fault patch ruptured by the Gorkha earthquake and the surrounding area of the MHT. The area East of the Gorkha earthquake last

ruptured in 1934 during a $M_w > 8.2$ earthquake. The return period of such events is estimated to be several centuries (e.g. Bollinger et al., 2014). So, it is probable that the stress level in that area has not yet recovered the 1934 stress drop, making a large event in that area improbable. The area updip and West of the Gorkha earthquake, which appeared nearly fully locked in the inter-seismic period, are more at risk given the lack of large earthquakes there over more than 500 yr. The only known historical earthquake which potentially ruptured the shallower portion of the MHT, updip, of the Gorkha rupture is the 1866 event which is estimated to have reached M_w 7.2 (Szeliga et al., 2010). The last large earthquake which ruptured the MHT at the surface West of Kathmandu occurred in 1344 (Bollinger et al., 2016). Farther West the last rupture occurred in 1505 (Yule et al., 2006; Ambraseys and Douglas, 2004; Mugnier et al., 2013; Hossler et al., 2016). The ~ 10 m deficit of slip that has built up since these events, given the

~20 mm/yr long term slip rate and assuming the fault has remained locked over the entire inter-seismic period, probably exceeds the amount of slip released by these earthquakes. These areas are clearly at risk of large earthquakes in the future, possibly as large as $\mathcal{M}_w 9.0$ (Stevens and Avouac, 2016).

5. Conclusions

The GPS time series before and after the Gorkha (Nepal) 2015 earthquake show a mixed contribution from secular inter-seismic loading, seasonal variations driven by surface hydrology, co-seismic and transient post-seismic deformation. The investigation of the post-seismic deformation required separating these different factors. The vbICA method performed very well to that effect, allowing us to separate the seasonal and post-seismic signals (see Fig. S1 of the Supplementary Material). The analysis of pre-seismic time-series did not reveal any detectable precursory signal. Our analysis of post-seismic deformation over the first 210 days after the mainshock shows that it was at least $76.7 \pm 1.0\%$ aseismic. The measured deformation is consistent with rate-strengthening frictional sliding on the MHT mostly downdip of the rupture. The afterslip zone reaches farther South and to shallower depth at the eastern end of the rupture, suggesting that the April 25th mainshock was interrupted by a rate-strengthening barrier. Afterslip there may have contributed to triggering the intense aftershock activity there, including the $\mathcal{M}_w 7.2$ aftershocks of May 12, 2015. The analysis presented here can be refined in future studies based on longer time series and by including more components than the first IC here analyzed. It is also possible that the deep afterslip patch reflects in fact some component of viscoelastic relaxation. The inclusion of additional geodetic data from Tibet should help resolve better the pattern of post-seismic deformation there and the nature of the relaxation mechanism.

Acknowledgment

The geodetic array of the Department of Mines and Geology (Nepal) was constructed and maintained thanks to Jean-Philippe Avouac's startup funds at the California Institute of Technology, and support from the Gordon and Betty Moore foundation to the Tectonics Observatory at Caltech. We also acknowledge support from the Département Analyse et Surveillance de l'Environnement (CEA, France). This work would not have been possible without the datasets acquired under two awards: (1) NSF EAR 1345136 to J.P. Avouac and N. Lapusta, at the California Institute of Technology (Galetzka et al., 2015); and (2) a NASA-funded supplement to the GAGE Facility award, under a request framed by J.P. Avouac for UNAVCO engineering support, data recovery and data services. UNAVCO is supported to operate the GAGE Facility by the National Science Foundation (NSF) and National Aeronautics and Space Administration (NASA) under NSF Cooperative Agreement No. EAR-1261833. The Department For Foreign International Development and the National Environment Research Council (UK) also provided support for the post-seismic response. Some of the figures have been created using the Generic Mapping Tools (GMT) software (Wessel and Smith, 1998). Victoria Stevens provided the coupling model and the fault geometry used in this work. Mathilde Radiguet provided some scripts used in the inversion of the geodetic data. We thank Romain Jolivet for discussion and Kristel Chanard for her insight regarding the modelling of the seasonal deformation. We thank the guest editor, Gavin P. Hayes, as well as Roland Bürgmann and one anonymous reviewer for the comments which improved the manuscript.

Appendix A

Following the approach and notation of Perfettini and Avouac (2004), the evolution with time t of post-seismic slip $\delta(t)$ of a velocity-strengthening 1-dimensional spring-slider system dragged at

a constant loading velocity V_0 is given by the equation:

$$\delta(t) = \delta_i + V_0 t_r \ln \left[1 + q \left(\exp \left(\frac{t}{t_r} \right) - 1 \right) \right] \quad (\text{A1})$$

where δ_i is a constant (arbitrary) value that we set equal to 0, q is a constant relating the apparent friction parameter, the normal stress acting on the patch, the effect of the shear stress variation on the slider and relates it to the loading velocity V_0 and the starting sliding velocity of the slider. Finally, t_r is the characteristic relaxation time.

The post-seismic slip evolution $\delta(t)$ is made up of two contributions: the afterslip due to the aseismic slip on the fault and the long-term creeping. We can thus split the left hand side of Eq. (A1) as

$$\delta(t) = \delta_{as}(t) + V_0 t. \quad (\text{A2})$$

The temporal evolution of the afterslip as deduced from the data ($\tilde{\delta}_{as}(t)$) starts from the first epoch available in the dataset (t_1). Thus, we set the corresponding temporal IC equal to 0 at time t_1 . This is equivalent to neglect the first t_1 days of deformation, i.e., it corresponds to say that the slip associated to the afterslip IC is:

$$\tilde{\delta}_{IC}(t) = \tilde{\delta}_{as}(t) - \tilde{\delta}_{as}(t_1). \quad (\text{A3})$$

Considering the modelled quantity $\delta_{as}(t)$ as a good representation of the quantity deduced from the data $\tilde{\delta}_{as}(t)$, we can rewrite the right hand side of Eq. (A3) using the model Eqs. (A2) and (A1):

$$\begin{aligned} \tilde{\delta}_{IC}(t) &= \tilde{\delta}_{as}(t) - \tilde{\delta}_{as}(t_1) \approx \delta_{as}(t) - \delta_{as}(t_1) \\ &= V_0 t_r \ln \left[\frac{1 + q \left(\exp \left(\frac{t}{t_r} \right) - 1 \right)}{1 + q \left(\exp \left(\frac{t_1}{t_r} \right) - 1 \right)} \right] - V_0 (t - t_1). \end{aligned} \quad (\text{A4})$$

Bringing the long-term factor to the left hand side, and dividing for V_0 both sides we get:

$$\frac{\tilde{\delta}_{as}(t) - \tilde{\delta}_{as}(t_1)}{V_0} + (t - t_1) \approx \frac{\delta_{as}(t) - \delta_{as}(t_1)}{V_0} + (t - t_1) = t_r \ln \left[\frac{1 + q \left(\exp \left(\frac{t}{t_r} \right) - 1 \right)}{1 + q \left(\exp \left(\frac{t_1}{t_r} \right) - 1 \right)} \right] \quad (\text{A5})$$

that is Eq. (7) in the main text.

Appendix B

Let us consider the Gutenberg–Richter law:

$$\text{Log} N = a - b \mathcal{M}_w \quad (\text{B1})$$

where N is the number of expected events having magnitude greater than \mathcal{M}_w , while a and b are constants.

Using the correspondence between seismic moment M_0 (in Nm) and moment magnitude \mathcal{M}_w described by the equation (Hanks and Kanamori, 1979):

$$\mathcal{M}_w = \frac{2}{3} \text{Log} M_0 - 6.07 \quad (\text{B2})$$

we can rewrite the Gutenberg–Richter law in terms of M_0 , and express the seismic moment as a function of N :

$$M_0 = \left(10^{a+6.07b} \right)^{\frac{3}{2b}} N^{-\frac{3}{2b}}. \quad (\text{B3})$$

This means that given a certain seismic moment M_{01} , we have N_1 earthquakes with a moment greater than M_{01} . Considering another

seismic moment $M_{02} < M_{01}$, it will be $N_2 > N_1$. To calculate the expected moment released by the events with moment in the range $[M_{02}, M_{01}]$ we have to integrate M_0 between N_1 and N_2 :

$$\nu_{1,2} = \int_{N_1}^{N_2} M_0(N) dN. \quad (B4)$$

If there is a finite number of aftershocks with moment between M_{01} and M_{02} and if they exactly follow the Gutenberg–Richter relationship, then the quantity $\nu_{1,2}$ gives us an overestimation of the seismic moment produced by the aftershocks. The result of such integral is:

$$\nu_{1,2} = \left(10^{a+6.07b}\right)^{\frac{3}{2b}} \frac{2b}{2b-3} N_{\frac{2b-3}{2b}}^{\frac{3}{2b}} \Big|_{N_1}^{N_2} \quad (B5)$$

The constant $\left(10^{a+6.07b}\right)^{\frac{3}{2b}}$ can be estimated looking at Eq. (B3). We can select a specific value for the seismic moment (M_{0*}) and count all the events (N_*) with a moment greater than the selected value. Thus, we can rewrite:

$$\nu_{1,2} = M_{0*} N_*^{\frac{3}{2b}} \frac{2b}{2b-3} N_{\frac{2b-3}{2b}}^{\frac{3}{2b}} \Big|_{N_1}^{N_2} \quad (B6)$$

Assuming the GCMT catalogue to be complete over a certain magnitude \bar{M}_w , we can select the set of K aftershocks having magnitudes above the completeness threshold and calculate an upper bound for the moment released by aftershocks as follows:

$$M_{0 \text{ aftershocks}}^{\text{tot}} \leq \sum_{k=1}^K M_{0k} + \nu_{K,\infty} \quad (B7)$$

where $\nu_{K,\infty}$ corresponds to the integral B4 using $N_1 = N_K = K + 1$, since we have K aftershocks and 1 mainshock, and $N_2 \rightarrow \infty$, that corresponds to consider all the aftershocks up to those with null seismic moment. Introducing for b a value of 1.0, typical for this region (Ader et al., 2012), and taking $N_1 = N_*$, we get:

$$M_{0 \text{ as}}^{\text{tot}} \leq \sum_{k=1}^K M_{0k} + 2(K+1)M_{0*}. \quad (B8)$$

Choosing a completeness magnitude $\bar{M}_{lw} = 5$, from the GCMT catalogue we have that $K + 1 = 9$, and $M_{0*} = 6.66 \times 10^{16}$ Nm (corresponding to a magnitude of $M_w = 5.146$). Thus, using also the moments of the other aftershocks in the catalogue, an upper bound for the total moment released by the aftershocks will be 11.824×10^{19} Nm. Before comparing this quantity with the moment released by afterslip we subtract the seismic moment released by the main aftershock since we have corrected the position time series for the effects of such event. We finally obtain as upper bound for the moment released by aftershocks the value of 2.984×10^{19} Nm. To perform all these calculation we consider errorless seismic moments since no uncertainties are provided in the GCMT catalogue.

Appendix C. Supplementary data

Supplementary data to this article can be found online at <http://dx.doi.org/10.1016/j.tecto.2016.06.014>.

References

Ader, T., Avouac, J.P., Liu-Zeng, J., Lyon-Caen, H., Bollinger, L., Galetzka, J., Genrich, J., Thomas, M., Chanard, K., Sapkota, S.N., Rajaure, S., Shrestha, P., Ding, L., Flouzat, M., 2012. Convergence rate across the Nepal Himalaya and interseismic coupling on the Main Himalayan Thrust: implications for seismic hazard. *J. Geophys. Res. Solid Earth* 1170 (B4). <http://dx.doi.org/10.1029/2011JB009071>.

Adhikari, L.B., Gautam, U.P., Koirala, B.P., Bhattarai, M., Kandel, T., Gupta, R.M., Timsina, C., Maharjan, N., Maharjan, K., Dahal, T., Hoste-Colomer, R., Cano, Y., Dandine, M.,

Guilhem, A., Merrer, S., Roudil, P., Bollinger, L., 2015. The aftershock sequence of the 2015 April 25 Gorkha-Nepal earthquake. *Geophys. J. Int.* 2030 (3), 2119–2124. <http://dx.doi.org/10.1093/gji/ggv412> (0).

Ambraseys, N.N., Douglas, J., 2004. Magnitude calibration of north Indian earthquakes. *Geophys. J. Int.* 10 (159), 165–206 0.

Avouac, J.P., Meng, L., Wei, S., Wang, T., Ampuero, J.P., 2015. Lower edge of locked Main Himalayan Thrust unzipped by the 2015 Gorkha earthquake. *Nat. Geosci.* 8 (9), 708–711. <http://dx.doi.org/10.1038/ngeo2518> (0).

Barbot, S., Fialko, Y., Bock, Y., 2009. Postseismic deformation due to the Mw 6.0 2004 Parkfield earthquake: stress-driven creep on a fault with spatially variable rate- and-state friction parameters. *J. Geophys. Res.* 1140 (B07405). <http://dx.doi.org/10.1029/2008JB005748>.

Bettinelli, P., Avouac, J.P., Flouzat, M., Bollinger, L., Ramillien, G., Rajaura, S., Sapkota, S., 2008. Seasonal variations of seismicity and geodetic strain in the Himalaya induced by surface hydrology. *Earth Planet. Sci. Lett.* 2660 (3–4), 332–344 0.

Bevis, M., Brown, A., 2014. Trajectory models and reference frames for crustal motion geodesy. *J. Geod.* 88, 283–311. <http://dx.doi.org/10.1007/s00190-013-0685-5> (0).

Bollinger, L., Sapkota, S.N., Tapponnier, P., Klinger, Y., Rizza, M., Van der Woerd, J., Tiwari, D.R., Pandey, R., Bitri, A., de Berc, S.B., 2014. Estimating the return times of great Himalayan earthquakes in eastern Nepal: evidence from the Patu and Bardibas strands of the Main Frontal Thrust. *J. Geophys. Res. Solid Earth* 1190 (9), 7123–7163 0.

Bollinger, L., Tapponnier, P., Sapkota, S., Klinger, Y., 2016. Slip deficit in central Nepal: omen for a repeat of the 1344 AD earthquake? *Earth, Planets Space* 680 (12).

Bürgmann, R., Kogan, M.G., Steblou, G.M., Hilley, G., Levin, V.E., Apel, E., 2005. Interseismic coupling and asperity distribution along the Kamchatka subduction zone. *J. Geophys. Res. Solid Earth* 1100 (B7).

Chanard, K., Avouac, J.P., Ramillien, G., Genrich, J., 2014. Modeling deformation induced by seasonal variations of continental water in the Himalaya region: sensitivity to Earth elastic structure. *J. Geophys. Res. Solid Earth* 1190 (6), 5097–5113 0.

Choudrey, R.A., 2002. Variational methods for Bayesian independent component analysis. *Pattern Analysis and Machine Learning – Robotics Research Group*. University of Oxford.

Choudrey, R.A., Roberts, S.J., 2003. Variational mixture of Bayesian independent component analyzers. *Neural Comput.* 150 (1), 213–252 0.

Denolle, M.A., Fan, W., Shearer, P.M., 2015. Dynamics of the 2015 M7.8 Nepal earthquake. *Geophys. Res. Lett.* 42 (18), 7467–7475 0.

Duputel, Z., Vergne, J., Rivera, L., Wittlinger, G., Farra, V., Hetényi, G., 2016. The 2015 Gorkha earthquake: a large event illuminating the Main Himalayan Thrust fault. *Geophys. Res. Lett.* 0 (43). <http://dx.doi.org/10.1002/2016GL068083>.

Dziewonski, A.M., Chou, T.A., Woodhouse, J.H., 1981. Determination of earthquake source parameters from waveform data for studies of global and regional seismicity. *J. Geophys. Res.* 0 (86), 2825–2852. <http://dx.doi.org/10.1029/JB086iB04p02825> (0).

Ekstrom, G., Nettles, M., Dziewonski, A.M., 2012. The global CMT project 2004–2010: centroid-moment tensors for 13,017 earthquakes. *Phys. Earth Planet. Inter.* 200–201 (0), 1–9. <http://dx.doi.org/10.1016/j.pepi.2012.04.002>.

Elliott, J.R., Jolivet, R., González, P.J., Avouac, J.P., Hollingsworth, J.C., Searle, M.P., Stevens, V.L., 2016. Geometry of the Main Himalayan Thrust fault and relation to topography revealed by the Gorkha earthquake. *Nat. Geosci.* 9 (0), 174–180. <http://dx.doi.org/10.1038/ngeo2623>.

Fu, Y.N., Freymueller, J.T., 2012. Seasonal and long-term vertical deformation in the Nepal Himalaya constrained by GPS and GRACE measurements. *J. Geophys. Res. Solid Earth* 1170 (B3). <http://dx.doi.org/10.1029/2011JB008925>.

Galetzka, et al., 2015. Slip pulse and resonance of Kathmandu basin during the 2015 Mw 7.8 Gorkha earthquake, Nepal imaged with geodesy. *Science* 3490 (6252), 1091–1095. <http://dx.doi.org/10.1126/science.aac6383> (0).

Grandin, R., Vallee, M., Satriano, C., Lacassin, R., Klinger, Y., Simoes, M., Bollinger, L., 2015. Rupture process of the M-w = 7.9 2015 Gorkha earthquake (Nepal): insights into Himalayan megathrust segmentation. *Geophys. Res. Lett.* 420 (20), 8373–8382. <http://dx.doi.org/10.1002/2015GL066044> (0).

Gualandi, A., Serpelloni, E., Belardinelli, M.E., 2014. Space–time evolution of crustal deformation related to the M_w 6.3, 2009 L’Aquila earthquake (central Italy) from principal component analysis inversion of GPS position time-series. *Geophys. J. Int.* 1970 (1), 174–191. <http://dx.doi.org/10.1093/gji/ggt522> (0).

Gualandi, A., Serpelloni, E., Belardinelli, M.E., 2015. Blind source separation problem in GPS time series. *J. Geodesy* 1–19 <http://dx.doi.org/10.1007/s00190-015-0875-4>.

Hanks, T.C., Kanamori, H., 1979. A moment magnitude scale. *J. Geophys. Res.* 840 (B5).

Hearn, E.H., Bürgmann, R., Reilinger, R.E., 2002. Dynamics of Izmit earthquake postseismic deformation and loading of the Duzce earthquake hypocenter. *Bull. Seismol. Soc. Am.* 920 (1), 172–193 0.

Hetland, E.A., Simons, M., 2010. Post-seismic and interseismic fault creep II: transient creep and interseismic stress shadows on megathrusts. *Geophys. J. Int.* 1810 (1), 99–112 0.

Hossler, T., Bollinger, L., Sapkota, S.N., Lave, J., Gupta, R.M., Kandel, T.P., 2016. Surface ruptures of large Himalayan earthquakes in Western Nepal: evidence along a reactivated strand of the Main Boundary Thrust. *Earth Planet. Sci. Lett.* 434 (0), 187–196.

Hsu, Y.J., Bechor, N., Segall, P., Yu, S.B., Kuo, L.C., Ma, K.F., 2002. Rapid afterslip following the 1999 Chi-Chi, Taiwan earthquake. *Geophys. Res. Lett.* 29. <http://dx.doi.org/10.1029/2002GL014967>.

Hsu, Y.J., Simons, M., Avouac, J.P., Galetzka, J., Sieh, K., Chlieh, M., Natawidjaja, D., Prawirodirdjo, L., Bock, Y., 2006. Friction afterslip following the 2005 Nias-Simeulue earthquake, Sumatra. *Science* 312 (0), 1921–1926.

Jouanne, F., Awan, A., Madji, A., Pecher, A., Latif, M., Kausar, A., Mugnier, J.L., Khan, I., Khan, N.A., 2011. Postseismic deformation in Pakistan after the 8 October 2005 earthquake: evidence of afterslip along a flat north of the Balakot-Bagh thrust. *J. Geophys. Res. Solid Earth* 1160 (B7).

Kaneko, Y., Avouac, J.P., Lapusta, N., 2010. Towards inferring earthquake patterns from geodetic observations of interseismic coupling. *Nat. Geosci.* 30 (5), 363–369 0.

- Kobayashi, T., Morishita, Y., Yaray, H., 2015. Detailed crustal deformation and fault rupture of the 2015 Gorkha earthquake, Nepal, revealed from ScanSAR-based interferograms of ALOS-2. *Earth Planets Space* 670 (2015).
- Kositsky, A.P., Avouac, J.P., 2010. Inverting geodetic time series with a principal component analysis-based inversion method. *J. Geophys. Res.* 1150 (B03401). <http://dx.doi.org/10.1029/2009JB006535>.
- Lin, Y.N., Sladen, A., Ortega-Culaciati, F., Simons, M., Avouac, J.P., Fielding, E.J., Brooks, B.A., Bevis, M., Genrich, J., Rietbrock, A., Vigny, C., Smalley, R., Socquet, A., 2013. Coseismic and postseismic slip associated with the 2010 Maule Earthquake, Chile: characterizing the Arauco Peninsula barrier effect. *J. Geophys. Res. Solid Earth* 1180 (6), 3142–3159 0.
- Lindsey, E.O., Natsuaki, R., Xu, X., Shimada, M., Hashimoto, M., Melgar, D., Sandwell, D.T., 2015. Line-of-sight displacement from ALOS-2 interferometry: Mw 7.8 Gorkha earthquake and Mw 7.3 aftershock. *Geophys. Res. Lett.* 420 (16), 6655–6661 0.
- Mahesh, P., Rai, S.S., Sivaram, K., Paul, A., Gupta, S., Sarma, R., Gaur, V.K., 2013. One-dimensional reference velocity model and precise locations of earthquake hypocenters in the Kumaon-Garhwal Himalaya. *Bull. Seismol. Soc. Am.* 1030 (1), 328–339 0.
- Marone, C.J., Scholz, C.H., Bilham, R., 1991. On the mechanics of earthquake afterslip. *J. Geophys. Res.* 960 (B5), 8441–8452 0.
- Monsalve, G., Sheehan, A., Rowe, C., Rajaure, S., 2008. Seismic structure of the crust and the upper mantle beneath the Himalayas: evidence for eclogitization of lower crustal rocks in the Indian Plate. *J. Geophys. Res. Solid Earth* 1130 (B8). <http://dx.doi.org/10.1029/2007JB005424>.
- Mugnier, J.L., Gajurel, A., Huyghe, P., Jayangondaperumal, R., Jouanne, F., Upreti, B., 2013. Structural interpretation of the great earthquakes of the last millennium in the central Himalaya. *Earth-Sci. Rev.* 127 (0), 30–47.
- Pandey, M.R., Tandukar, R.P., Avouac, J.P., Lave, J., Massot, J.P., 1995. Interseismic strain accumulation on the Himalaya crustal ramp (Nepal). *Geophys. Res. Lett.* 220 (7), 751–754 0.
- Perfettini, H., Ampuero, J.P., 2008. Dynamics of a velocity strengthening region: implications for slow earthquakes and postseismic slip. *J. Geophys. Res.* 1130 (B9). <http://dx.doi.org/10.1029/2007JB005398>.
- Perfettini, H., Avouac, J.P., 2004. Postseismic relaxation driven by brittle creep: a possible mechanism to reconcile geodetic measurements and the decay rate of aftershocks, application to the Chi-Chi earthquake. *J. Geophys. Res.* 1090 (B02304). <http://dx.doi.org/10.1029/2003JB002488>.
- Perfettini, H., Avouac, J.P., 2007. Modeling afterslip and aftershocks following the 1992 Landers earthquake. *J. Geophys. Res.* 1120 (B07409).
- Perfettini, H., Avouac, J.P., Tavera, H., Kositsky, A., Nocquet, J.M., Bondoux, F., Chlieh, M., Sladen, A., Audin, L., Farber, D.L., Soler, P., 2010. Seismic and aseismic slip on the Central Peru megathrust. *Nature* 4650 (6 May 2010). <http://dx.doi.org/10.1038/nature09062>.
- Radiguet, M., Cotton, F., Vergnolle, M., Campillo, M., Valette, B., Kostoglodov, V., Cotte, N., 2011. Spatial and temporal evolution of a long term slow slip event: the 2006 Guerrero slow slip event. *Geophys. J. Int.* 184 (0), 816–828. <http://dx.doi.org/10.1111/j.1365-246X.2010.04866.x>.
- Serpelloni, E., Faccenna, C., Spada, G., Dong, D., Williams, S.D.P., 2013. Vertical GPS ground motion rates in the Euro-Mediterranean region: new evidence of velocity gradients at different spatial scales along the Nubia–Eurasia plate boundary. *J. Geophys. Res. Solid Earth* 1180 (11), 6003–6024. <http://dx.doi.org/10.1002/2013JB010102> (0).
- Stevens, V., Avouac, J.P., 2015. Interseismic coupling on the main Himalayan thrust. *Geophys. Res. Lett.* 42 (14), 5828–5837 0.
- Stevens, V., Avouac, J.P., 2016. Millenary $M_w > 9.0$ earthquakes required by geodetic strain in the Himalaya. *Geophys. Res. Lett.* 43 (3), 1118–1123. <http://dx.doi.org/10.1002/2015GL067336>.
- Styron, R., Taylor, M., Okoronkwo, K., 2010. Database of active structures from the Indo-Asian collision. *Eos Trans. AGU* 910 (20), 181–182. <http://dx.doi.org/10.1029/2010EO200001> (0).
- Sun, T., Wang, K., 2015. Viscoelastic relaxation following subduction earthquakes and its effects on afterslip determination. *J. Geophys. Res. Solid Earth* 120 (0), 1329–1344. <http://dx.doi.org/10.1002/2014JB011707>.
- Szeliga, W., Hough, S., Martin, S., Bilham, R., 2010. Intensity, magnitude, location, and attenuation in India for felt earthquakes since 1762. *Bull. Seismol. Soc. Am.* 1000 (2), 570–584 0.
- Tapley, et al., 2005. GGM02—an improved earth gravity field model from GRACE. *J. Geod.* 790 (8), 467–478 0.
- Tarantola, A., 2005. *Inverse Problem Theory and Methods for Model Parameter Estimation*. SIAM.
- Wang, K., Fialko, Y., 2015. Slip model of the 2015 M-w 7.8 Gorkha (Nepal) earthquake from inversions of ALOS-2 and GPS data. *Geophys. Res. Lett.* 420 (18), 7452–7458 0.
- Wessel, P., Smith, W.H.F., 1998. New, improved version of the generic mapping tools released. *EOS, Trans. Am. Geophys. Union* 790 (579). <http://dx.doi.org/10.1029/98EO00426>.
- Yule, D., Dawson, S., Lave, J., Sapkota, S., Tiwari, D., 2006. Possible evidence for surface rupture of the Main Frontal Thrust during the great 1505 Himalayan earthquake, far-western Nepal.